JGR Solid Earth

RESEARCH ARTICLE
10.1029/2020JB019755

The Effects of Degassing on Magmatic Gas Waves and Long Period Eruptive Precursors at Silicic Volcanoes

Jacob S. Jordan[1,2], David Bercovici[1], Yang Liao[3], and Chloé Michaut[4,5]

[1]Department of Earth & Planetary Sciences, Yale University, New Haven, CT, USA, [2]Department of Earth, Environmental & Planetary Sciences, Rice University, Houston, TX, USA, [3]Woods Hole Oceanographic Institution, Falmouth, MA, USA, [4]Laboratoire de Géologie de Lyon, Ecole Normale Supérieure de Lyon, Université de Lyon, Paris, France, [5]Institut Universitaire de France (IUF), Paris, France

Key Points:
- A model for crystal-rich magma with exsolution of water vapor is developed to explain long period eruptive precursors at silicic volcanoes
- Sluggish kinetics for the exsolution of water favors the formation of porosity waves which may contribute to cyclical unrest
- Degassed crystal-rich magma is most susceptible to porosity waves

Correspondence to:
J. S. Jordan,
jj69@rice.edu

Citation:
Jordan, J. S., Bercovici, D., Liao, Y., & Michaut, C. (2020). The effects of degassing on magmatic gas waves and long period eruptive precursors at silicic volcanoes. *Journal of Geophysical Research: Solid Earth*, *125*, e2020JB019755. https://doi.org/10.1029/2020JB019755

Received 19 MAR 2020
Accepted 21 SEP 2020
Accepted article online 22 SEP 2020

Abstract Cyclical ground deformation, associated seismicity, and elevated degassing are important precursors to explosive eruptions at silicic volcanoes. Regular intervals for elevated activity (6–30 hr) have been observed at volcanoes such as Mount Pinatubo in the Philippines and Soufrière Hills in Montserrat. Here, we explore a hypothesis originally proposed by Michaut et al. (2013, https://doi.org/10.1038/ngeo1928) where porosity waves containing magmatic gas are responsible for the observed periodic behavior. We use two-phase theory to construct a model where volatile-rich, bubbly, viscous magma rises and decompresses. We conduct numerical experiments where magma gas waves with various frequencies are imposed at the base of the model volcanic conduit. We numerically verify the results of Michaut et al. (2013, https://doi.org/10.1038/ngeo1928) and then expand on the model by allowing magma viscosity to vary as a function of dissolved water and crystal content. Numerical experiments show that gas exsolution tends to damp the growth of porosity waves during decompression. The instability and resultant growth or decay of gas wave amplitude depends strongly on the gas density gradient and the ratio of the characteristic magma extraction rate to the characteristic magma degassing rate (Damköhler number, Da). We find that slow degassing can lead to a previously unrecognized filtering effect, where low-frequency gas waves may grow in amplitude. These waves may set the periodicity of the eruptive precursors, such as those observed at Soufrière Hills Volcano. We demonstrate that degassed, crystal-rich magma is susceptible to the growth of gas waves which may result in the periodic behavior.

1. Introduction

Periodic cycles of ground deformation, seismicity, and rapid dome-building eruptions have been observed at silicic volcanoes and are considered to be precursors of explosive eruptions. For example, both Mount Pinatubo in the Philippines and Soufrière Hills in Montserrat experienced periodic cycles of ground deformation and seismicity in 1991 and 1996–1997, respectively, with periods of about 10 hr at both volcanoes (Denlinger & Hoblitt, 1999; Lensky et al., 2008; Mori et al., 1996; Voight et al., 1999). Following the major eruption of 1991, Pinatubo experienced an increase in low-frequency seismicity, developing cyclic behavior with periods of 7–10 hr. At Soufrière Hills Volcano, the periodic activity was observed prior to episodes of rapid dome-building and major eruptive events. For examples of low-frequency seismicity observed at Pinatubo and Soufrière Hills Volcano, see Figure 1.

Several mechanisms for controlling this phenomenon have been proposed, including the stick-slip behavior of a crystalline plug atop the magma conduit (Anderson et al., 2010; Girina, 2013; Lensky et al., 2008; Mori et al., 1996; Voight et al., 1999). Periodic behavior has also been observed at other silicic volcanoes such as Volcan Santiaguito in Guatemala, where it is interpreted that magma flow, gas exsolution, and segregation pressurize a shallow region of the volcanic system beneath the vent (Johnson et al., 2014) or Sakurajima in Japan where the crystal-rich plug hypothesis remains the preferred explanation (Yokoo et al., 2013). As an alternative explanation for the cyclical occurrence of low-frequency seismicity, Michaut et al. (2013) proposed that porosity waves rising in the magma column are responsible for periodic behavior. The origin of porosity waves in the magma column could be the result of bubble accumulation during convection or heterogeneity in the magma chamber (Murphy et al., 1998; Parmigiani et al., 2016). Magma gas waves are effectively subjected to a band-pass filter during their ascent because of competition between gas expansion and compaction of the magma. Specifically, short wavelength gas waves are compressed by magma

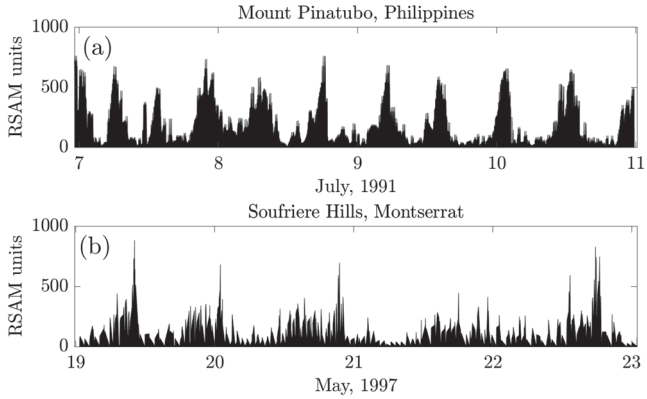

Figure 1. Cycles of high-intensity seismicity observed at two different silicic volcanoes. Real-time seismic amplitude measurements (RSAM) data are shown for Mount Pinatubo in the Philippines prior to the 1991 eruption and Soufrière Hills in Montserrat in 1997. At Pinatubo, elevated seismic activity was observed with a periodicity of 7–10 hr. At Soufrière Hills, periodic low-frequency seismicity was observed with periods of +6 hr. Data were extracted from Mori et al. (1996) and Voight et al. (1999).

compaction. Conversely, moderately long wavelength waves grow as gas expansion overcomes magma compaction. Very long waves do not grow as fast because gas escapes through overlying permeable magma more readily as it expands. Ultimately, the moderately long gas waves have the fastest growing amplitudes and are selected—or pass through the filter—eventually inducing the cyclical ground deformation that is observed.

Volatiles dissolved in magma, primarily dominated by water, play a crucial role in volcanic eruptions (Aiuppa et al., 2017; Huppert & Woods, 2002; Owen et al., 2013). Depressurization of volatile saturated melt results in the exsolution of volatile components, which increases the buoyancy of the magma column, thereby enhancing magma ascent (Eichelberger, 1995; Gardner, 2009; Gardner et al., 1995; Gonnermann & Manga, 2007; Huppert & Woods, 2002; Massol & Jaupart, 1999; Owen et al., 2013; Pistone et al., 2015). Additionally, increases in magma viscosity associated with degassing inhibit bubble coalescence and potentially limit volcanic degassing (Melnik & Sparks, 1999; Ruprecht & Bachmann, 2010; Sable et al., 2006), which can be further enhanced by degassing-induced crystallization. On the other hand, increasing gas exsolution rates or decreasing velocity of magma ascent may allow significant bubble coalescence and lead to permeable magma and more efficient volcanic degassing. Volcanic conduit models commonly assume that magma ascent is sufficiently slow such that the diffusion of volatile components into gas bubbles is not rate limiting and the gas and magma are in equilibrium (e.g., Melnik & Sparks, 1999). However, with magma ascent and volatile content varying, equilibrium may not always be maintained between gas bubbles and magma (Lyakhovsky et al., 1996; Mangan & Sisson, 2000; Navon et al., 1998). Recent, improved steady-state models for volcanic conduits consider the effects of magma degassing (Aravena & Vitturi, 2018; Aravena et al., 2017) but do not directly address effects that may arise from time-dependent variations in volatile exsolution. Although previous studies examine the effects of developing permeability in depressurized volatile-rich magma (Klug & Cashman, 1996; Saar & Manga, 1999) and changes in eruption style associated with changes in vesicularity and volatile content (Burton et al., 2007; Eichelberger et al., 1986; Woods & Koyaguchi, 1994; Wylie et al., 1999), it remains unclear how the rate of volatile exsolution and variations in local viscosity would affect the growth of porosity waves proposed by Michaut et al. (2013).

In this manuscript, we construct a theoretical model with the goal of elucidating how volatile release during magma ascent may play a role in exciting or dampening long period oscillations in volcanic processes (e.g., ground deformation). This conceptual model extends the theory of Michaut et al. (2013) to include disequilibrium degassing and its effect on volatile transport and local variations in magma viscosity. We use numerical models to examine how a range of volatile exsolution rates affect the growth of magma gas waves over a large range of wavelengths. We compare new numerical results to the results of Michaut et al. (2013) and identify an additional mechanism for gas wave selection that arises due to gas exsolution during magmatic ascent.

2. Theory

2.1. The Conceptual Model

We begin with a conceptual model wherein porosity waves containing compressible gas rise in a magma column. Upon arrival at the surface, porosity waves induce pore overpressurization resulting in episodic disturbances. We extend the theory of Michaut et al. (2013) to include dissolved water in melt exsolving to the gas phase and the associated effects on vesicularity, buoyancy, and melt viscosity. The magma column is assumed to be isothermal, due to the large heat capacity of magma (Bercovici & Michaut, 2010) but may be out of chemical equilibrium; for example, during depressurization, the magma may become supersaturated in water, which is exsolved into the gas phase. As water is released by the melt, the magma viscosity increases considerably (Giordano et al., 2008; Gonnermann & Manga, 2007; Hess & Dingwell, 1996). However, we do not consider melt density variations caused by changes in volatile content, which are on the order of a few percent (see and references therein Gonnermann & Manga, 2007).

Crystals are present throughout the eruption and contribute to rheological stiffening of the magma, and here are considered as passive cargo in the melt. If the crystal cargo does not reach a critical threshold, the form of the equations in theoretical model is not greatly affected. Thus, we neglect crystallization during magma ascent. Small amounts of crystallization ($\ll$10% by volume) may occur for continuous depressurization over relevant time scales (3–4 MPa hr^{-1}) for the effusively erupting silicic magma modeled in this study (Befus & Andrews, 2018). Other anhydrous phases such as pyroxenes will also crystallize during magma decompression. Therefore, crystallization of $\ll$10% by volume is a lower bound estimate. The potential dynamic effect of crystallization within our theoretical framework is discussed in detail later. Crystals carried by the ascending magma do not exchange dissolved water with the magma or gas phase (Barmin et al., 2002).

In previous studies (e.g., Mori et al., 1996; Yokoo et al., 2013) of ultra-low-frequency periodicity, cyclic behavior is often related to the geometry of the conduit, a stiffened magma in the form of a crystal-rich plug and the associated friction between them. Thus, it should be expected that, in events sensitive to the shallow volcano plumbing geometry such as dome collapse, reshaping of the conduit from explosive events or erosion via viscous dissipation near conduit walls will lead to significant variations in cycle frequency. However, once ultra-low-frequency periodic behavior is established, significant variations in cycle frequency are not observed. To examine the physics of the system that are insensitive to conduit geometry, we neglect conduit wall drag and focus on changes in the properties of the magma-gas mixture due to water exsolution from the melt during ascent. The ascending magma-gas mixture behaves as a shear-thinning, non-Newtonian fluid that rises in the conduit as a stiff, columnar plug rather than traditional Poiseuille flow appropriate to describe Newtonian fluids in a pipe (Gonnermann & Manga, 2007; Jellinek & Bercovici, 2011). Given the shear-thinning nature of the mixture close to the walls and the modest magma ascent rate (e.g., ~0.01 m s^{-1} during effusive periods of dome building at both Pinatubo and Soufrière Hills Volcano; see Cassidy et al., 2018 and references therein), the effect of wall friction only partially mitigates the buoyancy forces acting on the magma in the center of the column (Michaut et al., 2009). In this study, we seek to understand a process by which porosity waves grow or decay as a function of their wavelength. However, we acknowledge that to construct a full conduit model where magma ascent accelerates significantly, triggering a change in eruptive behavior, wall drag is an essential portion of the physics that should be considered.

Vesicularity at the base of the conduit may vary owing to convection in the underlying magma chamber, which promotes bubble accumulation in the crystal poor, top of the underlying magma chamber (Parmigiani et al., 2016). The dissolved water content in magma at the base of the conduit may vary slightly due to heterogeneity within magma chamber, episodic recharge, or uneven degassing from variations in temperature during convective mixing in the porous magma chamber mush (Caricchi & Blundy, 2015; Caricchi et al., 2014; Cashman et al., 2017; Murphy et al., 1998).

A summary of parameters and calculated scaling quantities tested in numerical models are given in Table 1, and a schematic of the conceptual model model is shown in Figure 2.

2.2. Basic Equations

The one-dimensional continuity equations for magma and gas are

$$\frac{\partial \rho_m(1-\phi)}{\partial t} + \frac{\partial \rho_m(1-\phi)w_m}{\partial z} = -\Gamma, \tag{1}$$

Table 1
Symbology, the Full Range of Parameter Values, and Calculated Scaling Quantities Tested in Numerical Models

Variable	Description	Value	Dimensions
$[\cdot]'$	Superscript indicating dimensionless quantity	(–)	(–)
z	Vertical spatial coordinate	(–)	m
t	Time	(–)	s
ρ_m	Magma density	2,500	kg m^{-3}
ρ_g	Gas density	(–)	kg m^{-3}
ρ_0	Reference gas density, ($z = 0$)	(200, 500)	kg m^{-3}
ϕ	Gas fraction	(–)	(–)
ϕ_0	Reference gas fraction, ($z = 0$)	(0.1, 0.3)	(–)
r_c	Characteristic bubble radius	(10^{-5}, 10^{-3})	m
ϕ_c	Gas fraction characteristic bubble radius	(10^{-5}, 10^{-3})	m
r_b	Bubble radius	$r_c(\phi/\phi_c)^{1/3}$	m
w_m	Vertical magma velocity	(–)	m s^{-1}
w_g	Vertical gas velocity	(–)	m s^{-1}
P_g	Gas pressure	(–)	Pa
C_g	Sound speed of gas	(650, 1,000)	m s^{-1}
Γ	Mass transfer	(–)	kg m^{-3} s^{-1}
ϑ	Crystal fraction of magma	(0, 0.5)	(–)
ϑ_p	Packing volume fraction of crystals	(0.6, 0.9)	(–)
b	Einstein coefficient for dilute suspensions	2.5	(–)
X_l	Mass fraction of water dissolved in liquid, ($z = 0$)	$\mathcal{S}(\rho_0/\rho_m)^n$	(–)
γ	Volatile weakening constant for liquid	(0, 100)	(–)
μ_l^{wf}	Shear viscosity of water-free liquid	(10^7, 10^{10})	Pa s
μ_m	Shear liquid viscosity	(–)	Pa s
μ_g	Shear viscosity of gas	10^{-5}	Pa s
μ_m	Shear magma viscosity	(–)	Pa s
$\mathcal{G}$	Pore geometry constant	4/3	(–)
$k(\phi)$	Magma permeability	(–)	m^2
k_0	Reference permeability of magma	10^{-12}	m^2
s	Saturation coefficient for volatile in magma	4.11×10^{-6}	Pa^{-n}
n	Gas pressure exponent for water solubility	1/2	(–)
$\mathcal{W}$	Magma injection velocity, ($z = 0$)	(0.01, 0.1)	m s^{-1}
c_j	Magma-gas drag coefficient ($j \in [\mathrm{D}, \mathrm{St}]$)	(–)	(Pa s) m^{-2}
c_{D}	Darcy drag coefficient	μ_g/k_0	(Pa s) m^{-2}
c_{St}	Stokes drag coefficient	$(3\mu_l\phi^{1/3})/(r_c/\phi_c^{1/3})^2$	(Pa s) m^{-2}
$\delta_{j,0}$	Reference compaction length for Darcy or Stokes drag	$(\mathcal{G}\mu_m^{\mathrm{wf}}/c_j)^{1/2}$	m
t_a	Characteristic advective time scale	$\delta_{j,0}/\mathcal{W}$	s
t_R	Characteristic degassing time scale	(10, 10^5)	s
Da	Damköhler number	t_a/t_R	(–)
$\mathcal{S}$	Scaled water saturation of magma	$sC_g^{2n}\rho_m^n$	(–)
X_0	Basal volatile content, ($z = 0$)	$\mathcal{S}(\rho_0/\rho_m)^n$	(–)
α_j	Magma-gas segregation parameter	$\mathcal{W}c_j/(\rho_m g)$	(–)
β_j	Gas compressibility parameter	$C_g^2/g\delta_{j,0}$	(–)
$\mathcal{C}$	Analytical growth rate for linearized governing equations	(–)	s^{-1}
q	Numerical growth rate for full governing equations	(–)	s^{-1}

Note. Variations in model parameters are noted in text within figures and accompanying captions.

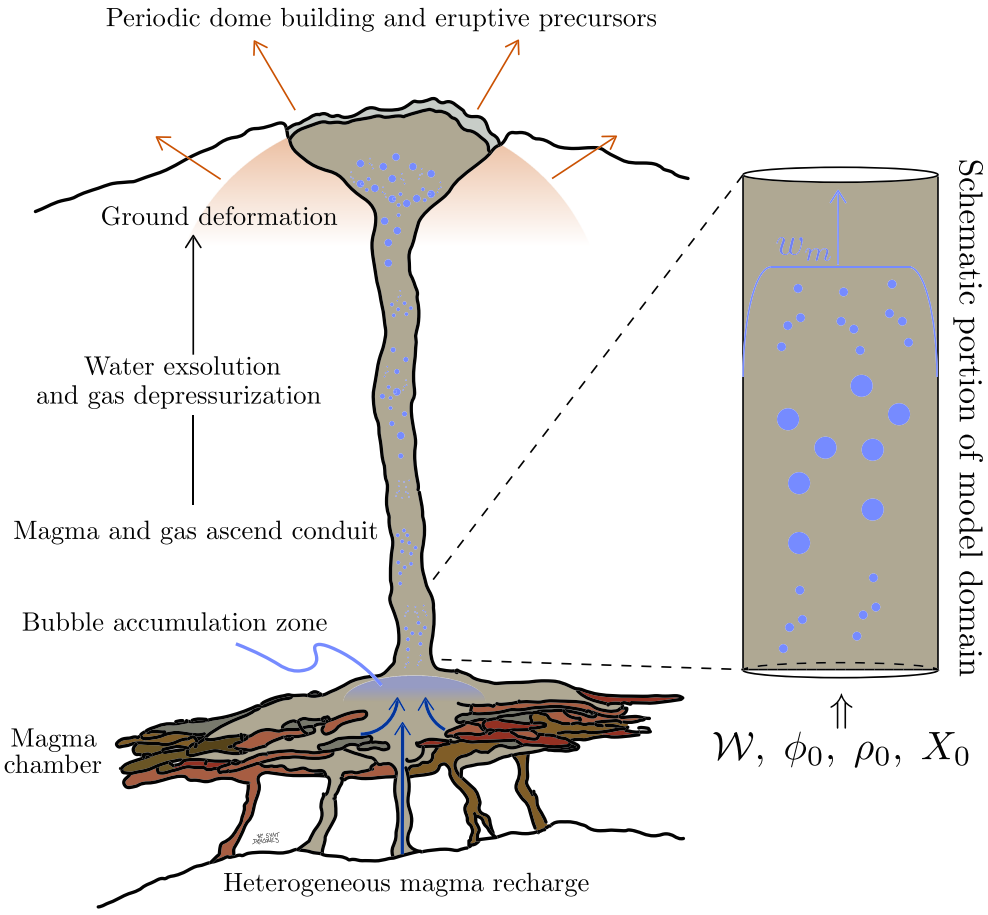

Figure 2. A schematic diagram for the conceptual model of a silicic volcano and corresponding simplified model domain. In the conceptual model, magma chamber recharge and convection may lead to small variations in gas fraction and dissolved water in magma. The magma and gas mixture enters the domain with initial vertical velocity, $\mathcal{W}$, gas density ρ_0, gas fraction ϕ_0, and weight percent of water dissolved in the melt portion of the magma mixture, X_0. The magma flows upward as a plug in the conduit, owing to the shear-thinning properties of the melt, crystal, and gas mixture (Gonnermann & Manga, 2007). Thus, in the conceptual model for effusive periods of eruption, we neglect conduit wall drag. As the magma and gas ascend, decompression leads to gas expansion and volatile exsolution. In the shallow subsurface and lava-dome portion of the volcanic system, variations in gas content and overpressure lead to ground deformation and the periodic real-time seismic amplitude measurements (RSAM) signals observed in Figure 1.

$$\frac{\partial \rho_g \phi}{\partial t} + \frac{\partial \rho_g \phi w_g}{\partial z} = \Gamma, \tag{2}$$

where, ϕ is the porosity, t is the time, z is the vertical coordinate, ρ_i is the density, and w_i is the velocity of phase $i \in [m, g]$, in which m and g denote the magma and gas phases, respectively. The magma phase is comprised of liquid melt and solid crystals that travel together at velocity w_m. The density of crystals and melt are assumed equal, ($\rho_m = \rho_{\text{crystal}} = \rho_{\text{liquid}}$), and all crystallizations are assumed to occur in the magma chamber (i.e., ascent-driven crystallization is neglected). This implies that the crystalline portion of the magma, ϑ, is constant. The right-hand sides of Equations 1 and 2 represent mass transfer due to gas exsolution and are discussed in detail below.

The gas pressure, P_g, obeys the ideal gas law

$$\rho_g = P_g / C_g^2, \tag{3}$$

where

$$C_g = \sqrt{RT/M}, \tag{4}$$

is the isothermal sound speed in which R is the ideal gas constant, T is temperature, and M is the molar mass of the gas. Equations 1 and 2 are similar to those presented in Michaut et al. (2013) with the addition of a mass transfer term (Γ).

Conservation of mass for the water dissolved in the liquid component of the magma is

$$\frac{\partial \rho_m(1-\phi)(1-\vartheta)X_l}{\partial t} + \frac{\partial \rho_m(1-\phi)(1-\vartheta)X_l w_m}{\partial z} = -\Gamma, \tag{5}$$

where X_l is the mass fraction of water dissolved in the liquid portion of the magma and ϑ is the crystal fraction in the magma.

The force balance equations for gas and magma are respectively

$$-\phi C_g^2 \frac{\partial \rho_g}{\partial z} - \phi \rho_g g + c_j \Delta w = 0, \tag{6}$$

$$-(1-\phi)\frac{\partial P_m}{\partial z} - (1-\phi)\rho_m g + \frac{\partial}{\partial z}\left[\frac{4}{3}\mu_m(1-\phi)\frac{\partial w_m}{\partial z}\right] - c_j \Delta w + \Delta P \frac{\partial \phi}{\partial z} = 0, \tag{7}$$

where P_m is the magma pressure, μ_m is magma viscosity, and g is gravitational acceleration (Michaut et al., 2013). The term c_j represents the interaction force between phases and is discussed in detail below. We also adopt the convention $\Delta x = x_m - x_g$ for any quantity x. In Equation 7, conduit wall drag is neglected. Following Michaut et al. (2009), we assume that variations in velocity along the vertical coordinate z are small compared to the variations in velocity across the width of the conduit. In the results presented here, wall friction would only partially offset a small portion of the buoyancy force acting on the magma. For details, see Michaut et al. (2009).

After Bercovici and Ricard (2003), the pressure difference in a viscously compacting magma matrix (neglecting surface tension) is

$$\Delta P = -\mathcal{G}\frac{\mu_m}{\phi}\frac{\partial w_m}{\partial z}, \tag{8}$$

where $\mathcal{G} \sim 1$ is a constant associated with pore geometry which is taken to be 4/3 for spherical pores (e.g., Yarushina & Podladchikov, 2015). The relationship (Equation 8) is akin to the bulk viscosity formulation of McKenzie (1984). The interaction force between the gas and magma matrix is characterized by the drag coefficient $c_j \in [c_{\mathrm{St}}, c_{\mathrm{D}}]$ for either Stokes' or Darcy drag. Consequences of different flow regimes on the selection of drag coefficient are discussed below after we introduce descriptions of volatile dependent melt viscosity and mass transfer from the liquid portion of the magma to the gas phase (i.e., degassing). The weighted difference of the force balance equations ($(1-\phi) \times (6)$ minus $\phi \times (7)$) is combined with Equation 8 yielding,

$$\frac{\partial}{\partial z}\left[\frac{4}{3}\mu_m \frac{1-\phi^2}{\phi}\frac{\partial w_m}{\partial z}\right] - (1-\phi)\Delta\rho g - \frac{c_j}{\phi}\Delta w = 0. \tag{9}$$

The magma viscosity is modeled assuming a suspension of rigid crystals in melt, following Krieger and Dougherty (1959)

$$\mu_m = \mu_l\left(1 - \frac{\vartheta}{\vartheta_p}\right)^{-b\vartheta_p}, \tag{10}$$

where b is the Einstein coefficient for dilute suspensions and ϑ_p is the maximum packing volume fraction of crystals. The Einstein coefficient has a theoretical value of $b = 2.5$ (Jeffrey & Acrivos, 1976). For packing of spheres of various sizes, ϑ_p may range from ~0.6 to 0.9 for applications to volcanic systems (Costa, 2005), and it is assumed that $\vartheta_p < 1$ to avoid magma viscosity reaching infinity or taking negative and imaginary values depending on the Einstein coefficient.

In this theoretical model, all significant crystallizations are assumed to occur within the magma chamber prior to transport up the conduit. In reality, as the melt phase expels water due to depressurization, the liquidus and solidus surfaces change, resulting in the growth of microlite crystals. In the case of Pinatubo, previous experimental studies and detailed calculations for microlite growth suggest that the magma may

increase in the crystal load during ascent (Andrews & Befus, 2020; Befus & Andrews, 2018; Hammer & Rutherford, 2002). However, for continuous decompression rates of 1–5 MPa hr^{-1}, this effect has little influence on Equations 5–10. By inspection of Equation 5, it is apparent that increasing crystal fraction, ϑ, at constant dissolved water content, X_l, forces a change in the mass transfer term, Γ, in order to maintain mass balance. As ϑ increases, the liquid portion of the magma becomes more oversaturated in water, resulting in faster water exsolution from the magma. For details on the disequilibrium relationship governing the exsolution of water from the liquid, see Equation 13 below. For the equation describing magma viscosity as a function of crystal content, Equation 10, an increase in ϑ results in higher viscosity but does not significantly alter the form of the equation as long as the crystal content does not approach the packing density for crystals (i.e., $\vartheta < \vartheta_p$).

The viscosity of liquid, μ_l, is assumed to be variable and a function of dissolved water in the liquid portion of the magma content according to

$$\mu_l(X_l) = \mu_l^{\mathrm{wf}} \times 10^{-\gamma X_l}, \tag{11}$$

where μ_l^{wf} is water-free liquid viscosity. Equation 11 is a linearization of Hess and Dingwell (1996) appropriate for magma with a dissolved water content ranging between 1% and 4%. To fit both the "strong" model of Hess and Dingwell (1996) and the "weak" model of Shaw (1965), we allow a range of liquid viscosity where $\gamma \in [0, 100]$ (Massol & Jaupart, 1999). For the case of $\gamma = 50$, the liquid viscosity changes by half of an order of magnitude with each weight percent variation in water, which is equivalent to the model of Hess and Dingwell (1996). The time required to obtain a numerical solution to the governing equations increases exponentially with increasing γ because more strict time discretization is necessary to resolve increasingly large viscosity contrasts in the magma (see Šrámek et al., 2010). Together, Equations 10 and 11 give a simplified model for the viscosity of the magma

$$\mu_m = \left(\mu_l^{\mathrm{wf}} \times 10^{-\gamma X_l}\right)\left(1 - \frac{\vartheta}{\vartheta_p}\right)^{-b\vartheta_p}. \tag{12}$$

The full and more complex relationship for magma viscosity is described by Hess and Dingwell (1996) (see Giordano et al., 2008; Gonnermann & Manga, 2007; Massol & Jaupart, 1999). We elect this simple formulation for analytical clarity. Our results later demonstrate that local changes in magma viscosity are of secondary importance compared to degassing for the growth of porosity waves.

To close the system of equations, an expression for the mass transfer term, Γ, is required. We assume linear disequilibrium so:

$$\Gamma = \frac{\rho_m}{t_R}\left(X_l - sP_g^n\right), \tag{13}$$

where t_R is the characteristic time scale for the kinetics of the reaction, s is the solubility constant for water in silicic magma (typically $s = 4.11 \times 10^{-6}$ for silicic magma with units of P^{-n}), and n is an exponent governing the gas-pressure dependence of water solubility (typically $n = 1/2$). We formulate Equation 13 after Kozono and Koyaguchi (2010) where the equilibrium gas exsolution is fitted on the basis of the solubility curve of water in silicic magma (Burnham & Davis, 1974). As kinetics become infinitely fast, $t_R \to 0$, the system is at chemical equilibrium so $X_l = sP_g^n$. We assume homogeneous bubble growth and explore a range of t_R where characteristic degassing proceeds on time scales of minutes to days. Such time scales are appropriate for andesitic to rhyolitic magma at high temperature (Bagdassarov et al., 1996; Navon et al., 1998).

For permeable magma, we assume a Darcian drag coefficient

$$c_j = c_{\mathrm{D}} = \frac{\mu_g \phi^2}{k(\phi)}, \tag{14}$$

where μ_g is gas viscosity and $k(\phi)$ is the permeability of the magma as a function of gas fraction. We express permeability via the relationship,

$$k(\phi) = k_0 \phi^2, \tag{15}$$

where k_0 is a reference permeability for vesicular magma (Klug & Cashman, 1996; Saar & Manga, 1999). Thus, the Darcy drag coefficient becomes

$$c_{\mathrm{D}} = \frac{\mu_g}{k_0}, \tag{16}$$

which is assumed constant despite the gas being compressible. At low gas fraction, bubbles are not connected, and the interaction between the gas and magma follows Stokes' law. In this case, bubbles interact with the liquid portion of the magma via the Hadamard-Rybczynski equation in the limit where $\mu_g \ll \mu_l$

$$c_j = c_{(\mathrm{St},0)} = 3\frac{\mu_l}{r_b^2}\phi, \tag{17}$$

where r_b is the characteristic radius of bubbles rising in the liquid (Batchelor & Batchelor, 2000; Michaut et al., 2013; Rybczynski, 1911). If the number density of bubbles remains constant, bubbles are allowed to grow due to gas decompression and water exsolving from the magma

$$r_b = r_c\left(\frac{\phi}{\phi_c}\right)^{1/3}. \tag{18}$$

Here, r_c is the bubble radius at a characteristic gas fraction ϕ_c. The drag coefficient depends on gas fraction following

$$c_{\mathrm{St}} = \frac{3\mu_l\phi^{1/3}}{\left(r_c/\phi_c^{1/3}\right)^2} = c_{(\mathrm{St},0)}\phi^{1/3}. \tag{19}$$

2.3. Characteristic Scales and Dimensionless Equations

A characteristic length-scale commonly used in the study of deformable porous media is the "compaction length" (Fowler, 1985; McKenzie, 1984)

$$\delta_{j,0} = \sqrt{\mathcal{G}\frac{\mu_m^{\mathrm{wf}}}{c_j}}, \tag{20}$$

where

$$\mu_m^{\mathrm{wf}} = \mu_l^{\mathrm{wf}}\left(1 - \frac{\vartheta}{\vartheta_p}\right)^{-b\vartheta_p}. \tag{21}$$

Although $\delta_{j,0}$ is constant, variations in magma viscosity may change the compaction length locally. The true local compaction length is

$$\delta_j = \left(\sqrt{\mu_m/\mu_m^{\mathrm{wf}}}\right)\delta_{j,0}. \tag{22}$$

Because the compaction length, $\delta_{j,0}$, scales proportionally with $c_j^{-1/2}$, it may vary drastically depending on the type of drag and the amount of dissolved water in the magma (Klug & Cashman, 1996; Michaut et al., 2009; Saar & Manga, 1999).

The magma and gas velocities are scaled by the injection velocity of magma at the base of the conduit, $\mathcal{W}$. The characteristic advective time scale is,

$$t_a = \delta_{j,0}/\mathcal{W}. \tag{23}$$

The independent and dependent variables of the system are therefore written as,

$$z = \delta_{j,0}z', \qquad w_i = \mathcal{W}w_i', \qquad t = t_a t'. \tag{24}$$

Densities and magma viscosity are likewise recast as

$$\rho_i = \rho_m\rho_i', \qquad \mu_m = \mu_m^{\mathrm{wf}}\mu_m', \tag{25}$$

where $\mu' = 10^{-\gamma X_m}$.

Substituting Equations 3, 24, and 25 into Equation 13 leads to the dimensionless mass transfer rate,

$$\Gamma' = \mathrm{Da}\left(X_l - \mathcal{S}\rho_g'^n\right), \tag{26}$$

where

$$\mathcal{S} = sC_g^{2n}\rho_m^n. \tag{27}$$

The ratio of the characteristic advective time scale to the exsolution time scale is called the Damköhler number

$$\mathrm{Da} = \frac{t_a}{t_R}. \tag{28}$$

The variables given by Equations 24 and 25 are substituted into Equations 1–7 to obtain the dimensionless governing equations which, omitting primes, are

$$\frac{\partial(1-\phi)}{\partial t} + \frac{\partial}{\partial z}\left[(1-\phi)w_m\right] = -\mathrm{Da}\left(X_l - \mathcal{S}\rho_g^n\right), \tag{29}$$

$$\frac{\partial\phi\rho_g}{\partial t} + \frac{\partial}{\partial z}\left[\phi\rho_g w_g\right] = \mathrm{Da}\left(X_l - \mathcal{S}\rho_g^n\right), \tag{30}$$

$$\frac{\partial(1-\phi)(1-\vartheta)X_l}{\partial t} + \frac{\partial}{\partial z}\left[(1-\phi)(1-\vartheta)X_l w_m\right] = -\mathrm{Da}\left(X_l - \mathcal{S}\rho_g^n\right), \tag{31}$$

$$-\beta_j\frac{\partial\rho_g}{\partial z} - \rho_g + \frac{\alpha_j}{\mathcal{F}_j(\phi)}\Delta w = 0, \tag{32}$$

$$\alpha_j\frac{\partial}{\partial z}\left[\mu_m\left(\frac{1-\phi^2}{\phi}\right)\frac{\partial w_m}{\partial z}\right] - (1-\phi)(1-\rho_g) - \frac{\alpha_j}{\mathcal{F}_j(\phi)}\Delta w = 0. \tag{33}$$

where

$$\alpha_j = \frac{\mathcal{W}c_j}{\rho_m g}, \tag{34a}$$

$$\beta_j = \frac{C_g^2}{g\delta_{j,0}}, \tag{34b}$$

and

$$\mathcal{F}_j(\phi) = \begin{cases} \mathcal{F}_{\mathrm{St}}(\phi) = \phi^{2/3} \\ \mathcal{F}_{\mathrm{D}}(\phi) = \phi \end{cases}. \tag{35}$$

The characteristic length scales may vary assuming a mixture of suspended bubbles rather than a permeable magma; however, it only changes the expression of the drag coefficient c_j. It is worth noting that changes in the drag coefficient do not significantly affect the governing equations (Michaut et al., 2013) or the results of following analysis presented in this manuscript. Scaling Equation 33, using Equations 18 and 19, results in a reference compaction length that depends on characteristic bubble radius

$$\delta_{(\mathrm{St},0)} = \left(\frac{1}{27}\right)^{1/2} r_c. \tag{36}$$

By inspection of Equation 36, it is apparent that the reference compaction length may be vanishingly small if the reference bubble radius associated with freshly nucleated tiny bubbles and may be on the order of cm if r_c is taken closer to the threshold wherein bubbles connect. If the characteristic length scale is the latter case, for a range of liquid viscosities, $\mu_l = 10^6$—10^9 Pa s, and gas viscosity, $\mu_g = 10^{-5}$ Pa s, the local compaction length, δ_j, calculated in Equation 20 may vary from centimeters to tens of meters.

The first dimensionless number, α_j, compares the characteristic magma ascent rate to the characteristic segregation velocity of gas percolating through magma. In effect, α_j determines the importance of compaction for expelling gas from the magma, as α_j becomes large, gas segregation due to magma compaction diminishes. The parameter β_j is a measure of gas compression due to hydrostatic pressure changes over a characteristic compaction length, where small β_j occurs for highly compressible gas.

Although changes in the drag coefficient do not significantly affect the governing equations of the mixture, the two dimensionless numbers are extremely sensitive to the drag coefficient and resultant compaction length. With increasing drag between phases, α_j increases, and thus, gas segregation decreases in importance. Similarly, with increased drag, the compaction length shortens which results in larger β_j, and the importance of gas compressibility diminishes. In the case of Stokes' flow $c_j = c_{\mathrm{St}}$, with small bubbles such that $r_b \to 0$, the compaction length becomes vanishingly small and $\beta_{\mathrm{St}} \to \infty$, making the gas effectively incompressible. The dimensionless number α_{St} calculated with a small characteristic bubble radius becomes extremely large, signifying that gas segregation is very small. In such a regime, the magma and gas mixture may be approximated as an incompressible, impermeable fluid with $\delta_{St} \approx 0$.

For permeable magma, where bubbles in the liquid phase connect, the drag coefficient, $c_j = c_{\mathrm{D}}$, is lower in comparison to the case appropriate for suspended bubbles (i.e., $c_j = c_{\mathrm{St}}$). The dimensionless number, α_j decreases for permeable magma indicating that gas segregation from the magma is significant. Furthermore, the increase in compaction length associated with lower drag results in smaller β_j which indicates that gas decompression upon the ascent of magma is significant.

If long period oscillations observed at volcanoes are in fact influenced by the selection of gas-rich porosity waves in decompressing magma, gas segregation and significant gas expansion are required. Michaut et al. (2013) demonstrate that such gas waves comprised of suspended bubbles may be able to grow on the scale of several tens of meters once gas bubbles become very large ($r_c \sim 1$ cm). Such waves of gas bubbles in magma (and beer) have been previously described by a balance between the growth of bubbles and hydrodynamic self-diffusion (see Manga, 1996; Watamura et al., 2019).

According to percolation theory, when bubble fraction of an unbounded fluid exceeds ~30%, interconnectedness of the inviscid phase is pervasive and porous flow ensues (Sahimi, 1994). However, this does not consider the presence of crystals and deformation of bubbles. Measurements for highly crystalline magma from Soufrière Hills Volcano, Mount Saint Helens, USA and Medicine Lake, USA samples show a gradual increase in permeability with increased vesicularity. The vesicle microstructure, bubble number density, and the resultant porosity-permability relationships depend on the deformation and decompression history of the magma. Bubble deformation by shearing and partial bubble collapse allows connectivity permeability and open-system degassing of magma with vesicularity of less than 20% (Rust & Cashman, 2004).

Once gas bubbles connect, waves of individual gas bubbles promptly decay or are absorbed by longer wavelength features due to the emergence of permeability and significant magma compaction. These longer wavelength permeable gas waves could be the source of the main trend for low-frequency periodic spikes in RSAM data at Pinatubo and Soufrière Hills Volcano (Figures 1 and 2). Michaut et al. (2013) demonstrated that meter-scale waves of smaller, suspended bubbles ($r_c < 1$ cm) would result in much higher frequency signals. Therefore, to explore the main trend of low-frequency periodic eruptive precursors at silicic volcanoes, we focus on a model framework featuring Darcy drag as opposed to Stokes drag. Henceforth, the subscript j is dropped from the drag coefficient and associated scales, so the presence of permeable magma and Darcy drag are assumed unless specified otherwise.

2.4. Steady-State Solution to Dimensionless Equations

Steady-state solutions for Equations 29–33 are obtained numerically. We assume that the mixture has compacted to an equilibrium gas fraction, ϕ_0, in the source magma chamber, and thus, on entering the conduit, there is little initial compaction, and subsequent compaction or dilation is mostly in response to gas exsolution and expansion during ascent. Thus, the bottom boundary condition for gas velocity is determined by assuming no compaction in Equation 33 and rearranging Δw to find

$$w_{g,0} = 1 + \frac{\phi_0(1-\phi_0)(1-\rho_0)}{\alpha}. \tag{37}$$

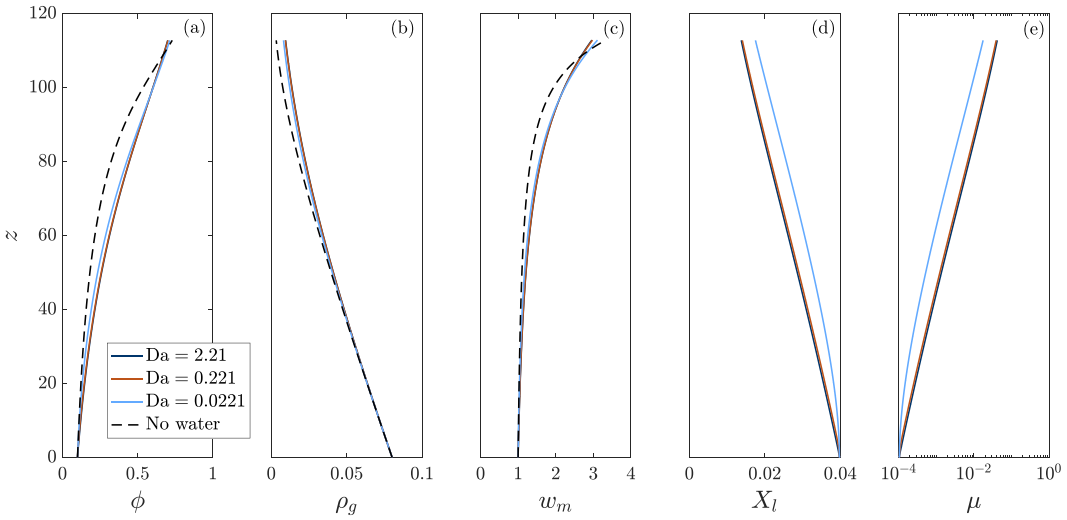

Figure 3. Dimensionless steady-state solutions to Equations 29–33 for three Damköhler numbers and water-free reference case similar to the results of Michaut et al. (2013). The characteristic magma ascent velocity is fixed at $\mathcal{W} = 0.02\,\mathrm{m\,s^{-1}}$ (Watts et al., 2002), but the exsolution rates are varied such that $t_R = 10^3$ (Navy), $t_R = 10^4$ (Orange) and $t_R = 10^5$ s (light blue). Dotted lines in (a)–(c) show water-free solutions for gas fraction and gas density. In these calculations, $\mu_l^{\mathrm{wf}} = 10^9$ Pa s, $\vartheta = 0.5$, $\vartheta_p = 0.6$, $\mu_g = 10^{-5}$ Pa s, $k_0 = 10^{-12}\,\mathrm{m^2}$, and $C_g = 685\,\mathrm{m\,s^{-1}}$. The gas fraction at the base of the conduit is $\phi_0 = 0.1$. The initial gas density is defined by $\rho_0 = \rho_g(z = 0) = 0.08\rho_m$. Lastly, the sensitivity of melt to dissolved water is parameterized by $\gamma = 100$. With these parameters, the dimensionless numbers (other than Da which is indicated) are $\alpha = 8.15$ and $\beta = 1.08 \times 10^3$. The volatile-free compaction length is $\delta_0 = 44.35$ m. A 5-km conduit ($\sim 113\delta_0$) is assumed.

In addition, we set $\phi = \phi_0$, $\rho_g = \rho_0$, and $w_m = 1$, at the base of the domain. The change in magma velocity is also found to be very small (Appendix C), and thus, for a second boundary condition on w_m, we set $\partial w_m/\partial z = 0$ at $z = 0$. Additionally, a bottom boundary condition is supplied for water dissolved in the melt at the base of the conduit, so $X_l = \mathcal{S}\rho_0^{1/2}$.

We find steady-state solutions by initializing $\phi = \phi_0$, $w_m = 1$, and $w_g = w_{g,0}$ throughout the column. We initialize the gas density and dissolved water profiles with $\rho_g = \rho_0 \exp(-bz/\rho_0)$ and $X_l = \mathcal{S}\rho_0^{1/2} \exp\left(-bz/\left(\mathcal{S}\rho_0^{1/2}\right)\right)$ to ensure positive values. After setting the initial and boundary conditions at the base of the conduit, we numerically integrate upward. At the top boundary, there is free outflow where both the gas and magma pressure remain slightly elevated above atmospheric pressure. This is because we only track magma evolution from the base of the column to the shallow subsurface, but not all the way to the surface. After setting the required initial and boundary conditions, the steady-state solutions are found using a finite volume method (see LeVeque, 2002).

2.5. Growth Rate of Magma Gas Porosity Waves

Michaut et al. (2013) show that porosity waves of specific wavelength are naturally selected by the competition between magma compaction and gas compressibility for a constant viscosity magma column without volatile exchange between melt and gas. Gas wave selection involves a broad band of wave frequencies where porosity wave amplitudes grow. Above a cut-off frequency, porosity wave amplitudes decay. Thus, the volcanic conduit acts as a low-pass filter for porosity waves. To explore the effect of degassing and variable magma viscosity on porosity wave selection—or filtering of porosity waves—we present time-dependent solutions to the governing Equations 29–33.

We perturb steady-state solutions by introducing boundary conditions where either oscillations in gas fraction, ϕ, or dissolved water in the melt, X_l, excite porosity waves. Oscillations are enforced at the bottom boundary such that

$$B = B_0\left(1 + A\sum_{j=1}^{n}\cos(2\pi f_j t)\right), \tag{38a}$$

$$\text{where} \quad B = \phi \quad \text{or} \quad B = X_l, \tag{38b}$$

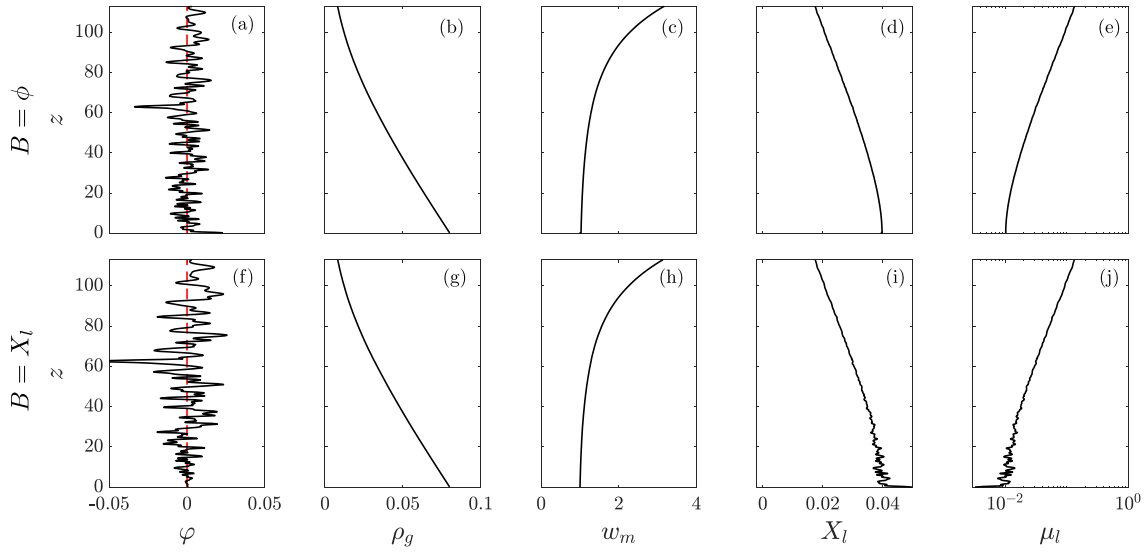

Figure 4. Comparison of end-member boundary conditions for the dimensionless time-dependent model described in Equation 38c. (a–e) Adjusted gas fraction, $\varphi = \phi - \phi_{ss}$, gas density, ρ_g, magma velocity, w_m, water dissolved in melt, X_l, and melt viscosity, μ_l, for case when $B = \phi$. (f–j) The same quantities for time-dependent model when $B = X_l$. In both simulations, material properties are equivalent to Figure 3, with the exception of the dependence of the viscosity on dissolved water which is here $\gamma = 50$. In both models, the bottom boundary oscillates with the superposition of 10 sinusoidal perturbations, f = [0.0266, 0.0620, 0.1682, 0.2036, 0.2568, 0.2745, 0.4692, 0.5932, 0.7348, 0.8942], and equal amplitudes of $A = 0.025$. The gas fraction at the bottom boundary is $\phi_0 = 0.1$ and $\rho_0 = 0.08\ \rho_m$. The volatile content at the bottom boundary oscillates around $X_0 = 0.0398$, the Damköhler number is Da = 0.0221, and a 5-km magma conduit is assumed in both simulations.

$$\text{and} \quad B_0 = \phi_0 \quad \text{or} \quad B_0 = X_0 = S\rho_0^n \quad \text{at} \quad z = 0. \tag{38c}$$

Here, A is the amplitude, and f_j is the frequency of the jth sinusoidal perturbation. Equations 32 and 33 are solved with the boundary conditions $w_m = 1$ and $\rho_g = \rho_0$ at $z = 0$ (Michaut et al., 2013), after which the magma, gas, and volatile mass equations are updated using Equations 29–31.

If periodic oscillations at the base of the conduit are imposed on gas fraction ϕ, then the volatile content is held constant, $X_l = S\rho_0^n = X_0$ at $z = 0$. For the values of $s = 4.11 \times 10^{-6}$ and $n = 1/2$, typically used for silicic melts, setting the dimensionless gas density, $\rho_0 = 0.08$ at $z = 0$, yields a dissolved water content of $X_0 = 3.98\%$ in the melt at the base of the conduit (as in Figure 3). Likewise, if dissolved water content oscillates around the equilibrium saturation value at the base, then $\phi = \phi_0$ at $z = 0$. To limit numerical diffusion in the time-dependent solutions, the monotonized-central-difference flux limiter method (LeVeque, 2002) is used for updating the conservation of mass equations. We compare these two boundary conditions to explore how gas wave filtering is affected by the presence of water and ongoing exsolution in the melt. To this end, time-dependent models (Figure 4) must be used to extract the growth rate of magma gas waves. We employ wavelike perturbations to represent magma chamber heterogeneity (as discussed in section 2.1), so we may exploit Fourier series to monitor the growth and decay of small porosity waves across a broad range of preprescribed frequencies. The periodic, wavelike perturbations are well suited for comparison to linear theory (Appendices A and B).

To calculate the growth rate of gas waves relative to the background steady state, we introduce an adjusted gas fraction

$$\varphi = \phi - \phi_{ss}, \tag{39}$$

where ϕ_{ss} is the steady-state gas fraction (Figures 4c and 4g). Assuming wavelike perturbations, the adjusted gas fraction may be represented as a Fourier series

$$\varphi(z,t) = \sum_{j=-N/2}^{N/2-1} \hat{\varphi}_j(z) e^{i2\pi f_j t}, \tag{40}$$

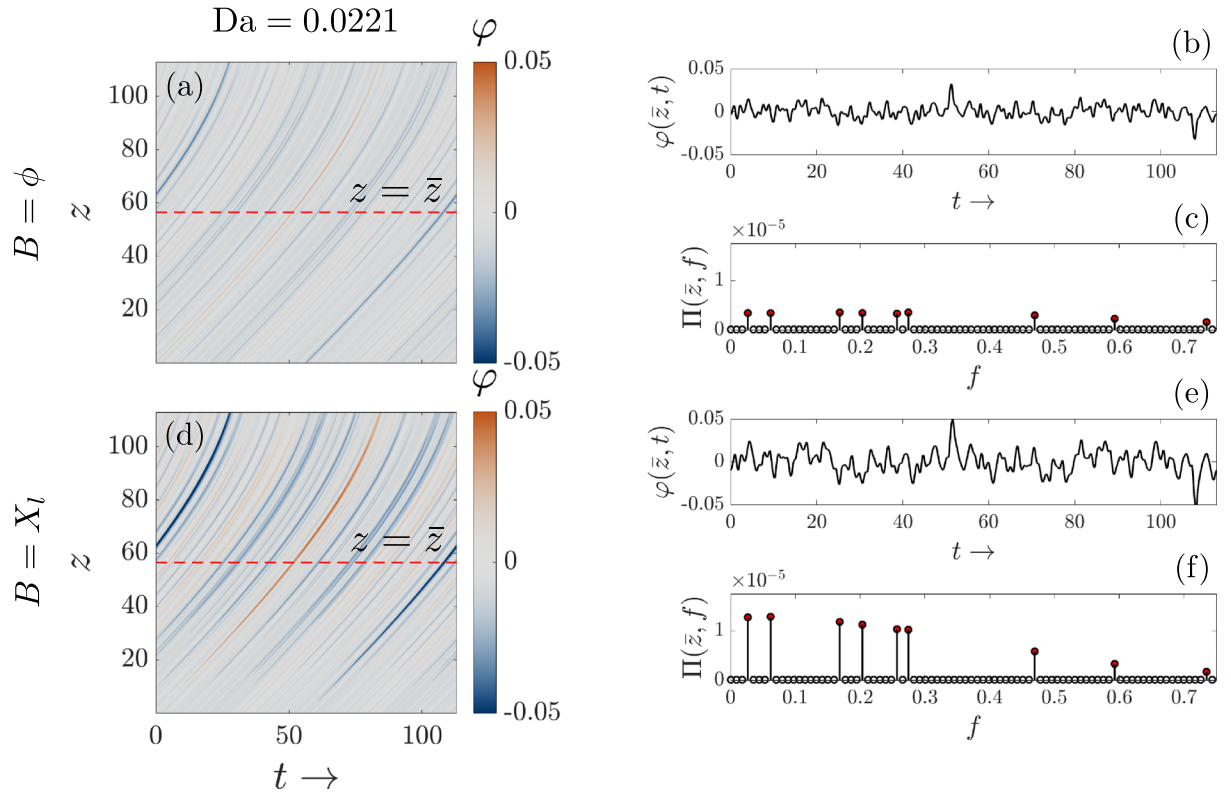

Figure 5. A discrete method for tracking wave growth. Panels (a) and (d) present the evolution of adjusted gas fraction, φ, presented in Figure 4 on the time interval $[0,(t_f - \Delta t)]$, where there are N time steps of size Δt. B indicates either oscillations in ϕ or X_l at the bottom boundary. In Panels (a) and (d), $t_f = 112.9$ and $\Delta t = 0.0113$. The red dashed line labeled $z = \bar{z}$ indicates the midpoint of the domain. Panels (b) and (e) track gas fraction at $z = \bar{z}$ though time. Panels (c) and (f) show the spectrum of adjusted gas fraction Π at $z = \bar{z}$. Panels (a)–(c) correspond to boundary conditions in Equations 38c where $B = \phi$, whereas (d)–(f) correspond to $B = X_l$. In both simulations, the bottom boundary oscillates with the superposition of ten sinusoidal perturbations as in Figure 4.

where $\hat{\varphi}_j$ is the discrete Fourier transform of φ at a given height, z, in time (Figures 5a, 5b, 5d, and 5e). We sample the time-dependent model output on an interval $[0, ((N-1)\times\Delta t)]$, where there are N time steps of equal size Δt. The power spectrum of φ for the jth frequency is

$$\Pi_j(z) = \hat{\varphi}_j(z)\hat{\varphi}_j^*(z), \tag{41}$$

where $\hat{\varphi}_j^*$ is the complex conjugate of $\hat{\varphi}_j$. An example of Π at a given height, $z = \bar{z}$, is plotted in Figures 5c and 5f. The power spectrum, Π_j, represents the portion of the signal at frequency f_j. At a given depth, $z = \bar{z}$, a higher power, Π_j, indicates that the signal is stronger at frequency f_j, while a lower power indicates that the signal is weaker. In the context of a series of superimposed gas waves, the power spectrum allows the quantification of wave amplitudes as a function of their frequency.

The growth or decay with height in the conduit for gas waves at the jth frequency is given by

$$q_j(z) = \frac{1}{2\Pi_j}\frac{d\Pi_j}{dz}. \tag{42}$$

When Π_j is calculated at multiple depths, $d\Pi_j/dz$ may be approximated to obtain a numerical measure for the instability of a gas wave, $q_j(z)$ (see Appendix A and Figures 6a and 6b). We calculate the root-mean-square envelope for the oscillations at each $q_j(z)$ and take the mean of the upper and lower bounds of the envelope to be the main trend in instability, which we refer to as $q(z)$ hereafter.

3. Results

As noted in Equation 38c, we consider two separate oscillating boundary conditions to induce magma gas waves. The methodology presented in section 2.5 and summarized in Figure 5 is used to compare the effect

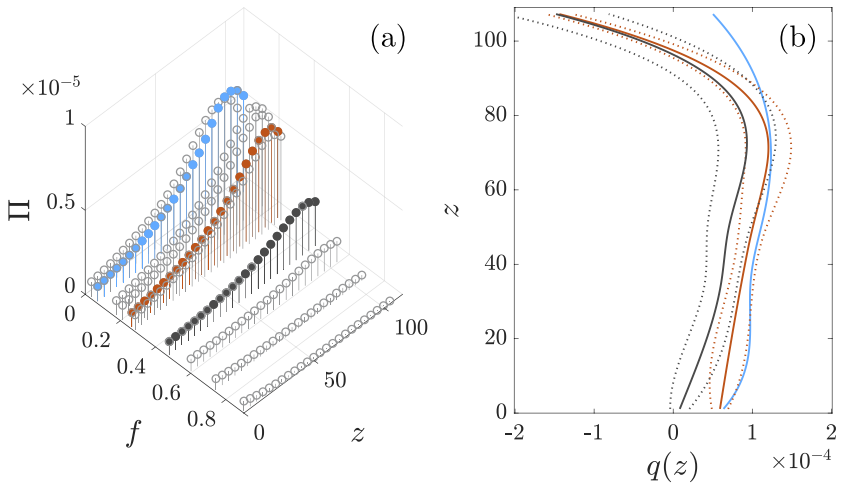

Figure 6. Relationship between Π and $q(z)$ in the conduit. (a) Demonstration of spectrum for gas fraction throughout the magma column. The spectrum was generated using solutions for φ where $X_l = \Gamma = 0$ and $B = \phi$. In this case, the dimensionless governing Equations 29–33 are equivalent to equations presented in Michaut et al. (2013). As in Figure 4, the bottom boundary oscillates with the superposition of 10 sinusoidal perturbations with equal amplitudes of $A = 0.025$. The gas fraction at the bottom boundary oscillates around $\phi_0 = 0.1$ and density is fixed at $\rho_0 = 0.08\rho_m$. Three frequencies ($f = 0.0620, 0.2568, 0.4692$) are highlighted to illustrate the relationship between Π and $q(z)$. (b) Calculated instability of gas waves $q(z)$. Solid lines show the mean trend of gas wave instability, $q(z)$, throughout the magma column. Dotted lines represent the variance in $q(z)$, forming an envelope that brackets oscillations in $q(z)$ about the mean. For the case where $f = 0.0620$ (light blue), the envelope is narrower than the width of the curve representing $q(z)$. Low variance in gas wave instability is typical of waves produced by low-frequency perturbations.

of the boundary conditions and gas exsolution rates on gas waves ascending through the magma column. First, we assume basal oscillations are only in gas fraction, ϕ. Next, we explore basal oscillations in X_l. We show that in either cases, the instability of gas waves is sensitive to the steady-state water content of the melt in the magma column. In the case of $B = X_l$, the formation of gas waves is highly sensitive to the Damköhler number. In either case, slow exsolution enhances the growth of low-frequency modes of gas waves relative to high-frequency modes.

Consider a magma conduit where basal perturbations in gas fraction induce porosity waves. From Equation 38c, $B = \phi$ at $z = 0$ similar to Michaut et al. (2013), although $X_l \neq 0$ and the assumption of local chemical equilibrium is relaxed. When magma enters the conduit bearing dissolved water, the amplification or decay of the gas porosity waves across a broad range of frequencies is affected substantially compared to the water-free model of Michaut et al. (2013).

When the exsolution of water from the melt to the gas phase is included in the conduit model, the sensitivity of gas wave stability, that is, the frequency-dependent growth or decay of Π, is apparent. Generally, the addition of dissolved water to the melt portion of the magma phase results in slower growth of porosity waves when compared to the exsolution-free model presented in Figure 6. Using material properties from Figure 3, the dissolved water content of melt at the base of the conduit is $X_0 = 3.98\%$. Using this value for X_0 but retaining the same time-dependent boundary condition used to generate the results of Figure 6, the maximum power of long wavelength gas waves is roughly halved (Figures 7a–7c). Meanwhile, short wavelength gas waves continue to decay rapidly, thereby flattening the overall trend for growth in Π. Small perturbations in gas fraction from Equation 38c have a negligible effect in changing local dissolved water content, X_l, and melt viscosity, μ_l, which remain close to their steady-state profiles (as in Figures 4a and 4b).

When the Damköhler number is decreased incrementally at constant X_0, we observe a slight increase in gas wave growth across all nondecaying modes. The tendency toward less wave growth occurs primarily due to decreasing gas density gradients in the magma column. With large Damköhler number, the rapid exsolution of water at the base of the conduit raises gas pressure. The smaller pressure drop over the length of the conduit results in less overall gas expansion. Steady-state solutions show that fast exsolution (i.e., large Da) suppresses gas density gradients more than slow exsolution, while water-free models display the largest gas density gradient (Figure 3b). Although the changes in gas density gradient with Da shown in Figure 3b

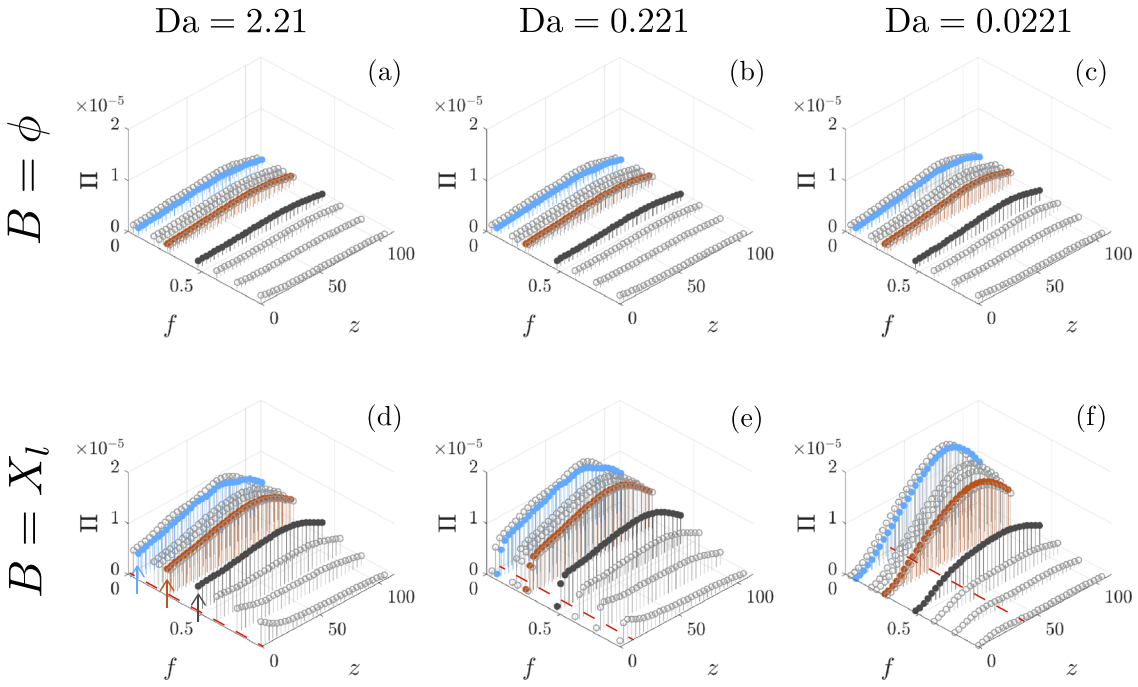

Figure 7. Demonstration of power spectrum, Π, for adjusted gas fraction, φ, throughout the magma column as Damköhler number, Da, varies across three orders of magnitude. As in Figures 4 and 5, the viscosity sensitivity parameter $\gamma = 50$. (a–c) The bottom boundary oscillates with the superposition of ten sinusoidal perturbations in ϕ where $\phi_0 = 0.1$ at $z = 0$ as in Figure 6. (d–f) In this suite of simulations, the water content of the melt oscillates around $X_0 = 0.0398$ where $\phi_0 = 0.1$ in Equation 38c with $B = X_l$. Three small arrows in (d) indicate the abrupt jump in Π near $z = 0$ when Da is large. In Panels (e) and (f), the exsolution of water is gradual and can be seen visualized by the smooth growth in Π with z. There are 10 sinusoidal perturbations of equal amplitude with frequencies matching Figure 4. Red dotted lines in (d)–(f) indicate the height in the column where degassing approaches a constant rate (see section 4.2). For convenience of comparison to Figures 6, the same three frequencies have been highlighted in light blue ($f = 0.0620$), orange ($f = 0.2568$), and gray ($f = 0.4692$). However, the z-axis for Π is now doubled compared with Figures 6 because small oscillations in X_l result in larger porosity waves.

may appear small, they translate to large changes in gas pore pressure depending on the compressibility of the gas ($P_g = C_g^2 \rho_g$). Due to the large drop in gas pore pressure, the moderately low-frequency modes that grow considerably when $X_l = 0$ may not increase in amplitude substantially when $X_l \neq 0$ as in Figure 7. Regardless, very short wavelength (or high-frequency) perturbations decay because gas expansion cannot compete with magma compaction.

Porosity wave instability is only weakly sensitive to changes in melt viscosity for small perturbations in gas fraction. Increasing the parameter γ in Equation 11 increases the sensitivity of melt viscosity to dissolved water, X_l. Simulations where melt viscosity remains constant despite variation in X_l (i.e., $\gamma = 0$) show qualitatively similar results to models where melt viscosity μ_l is affected substantially by local changes in dissolved water. Increasing γ results in very slight changes in moderately long wavelength porosity waves; however, these small changes do not recover the filtering effect demonstrated in Figure 6. In any case, the trend in gas wave selection as proposed by Michaut et al. (2013) is damped by the inclusion of dissolved water in melt when $B = \phi$.

We next allow magma at the base of the column to have oscillations in dissolved water content (Figures 7d–7f). For this case, we assume that magma enters the conduit with a constant gas fraction $\phi = \phi_0$. Oscillations at the base of the conduit proceed such that $B = X_l$ in Equation 38c and that the background water content of the melt is $X_0 = \mathcal{S}\rho_0^{1/2} = 3.98\%$ at $z = 0$. Unlike results presented in Figures 7a–7c, oscillations around the steady state induce substantial variations in melt viscosity, μ_l, (Figures 4a and 4b vs. 4e and 4f) and thus local compaction length, δ (Equation 22). A key difference between conduit models where $B = X_l$ versus $B = \phi$ is that gas waves formed by degassing require significant exsolution over finite time and space to grow within the conduit. Therefore, when $B = X_l$ the Damköhler number has a much stronger influence on the formation and growth selection of gas waves in the magma conduit than cases where $B = \phi$.

Degassing reduces the background gas pressure gradient in the conduit—thereby diminishing overall gas wave instability. However, when basal oscillations in water content push the magma-gas mixture far from

chemical equilibrium, gas waves form in the lower portion of the conduit from exsolution (e.g., Figure 4g). Here, we show that the frequency bandwidth of gas porosity waves that grow in the conduit is highly sensitive to Damköhler number.

Testing a range of exsolution rates reveals a new filtering effect separate from the gas wave selection mechanism reported in Michaut et al. (2013). When the Damköhler number is small, sluggish exsolution favors the growth of lower frequency perturbations which have sufficient time for the gas and melt to equilibrate. That is, water must be able to degas and regas from the melt allowing it to contribute to growth in the gas fraction via decompression expansion. The high-frequency modes of the volatile perturbation from Equation 38c oscillate too quickly for the gas and melt to equilibrate. Therefore, high-frequency modes contribute little to the gas fraction. The result is a well-defined trend where low-frequency porosity waves are accentuated with decreasing Damköhler number (compare Figures 7c and 7f). On the contrary, with Damköhler number sufficiently large, higher frequency perturbations may abruptly form owing to rapid degassing near the base of the conduit but are subsequently compacted away (Figure 7d).

Another key difference between models where $B = X_l$ and $B = \phi$ is that the power spectra of adjusted gas fraction, Π, start at zero for all models when $B = X_l$ (because $\phi = \phi_0$ at bottom boundary $z = 0$) and increase at a rate depending on the Damköhler number. For cases when the degassing time scale is long, higher frequency gas waves may not significantly form. When the Damköhler number is high, rapid degassing allows the formation of gas waves across a much broader band of frequencies (Figure 7d). However, the very short wavelength gas waves cannot be sustained over long distances because gas expansion is overwhelmed by magma compaction (e.g., Figures 7a–7d). In the suite of models presented in Figure 7, we find that changes in local melt viscosity has secondary importance to the selection of gas waves as is also the case when $B = \phi$. Therefore, for purpose of discussion, we proceed with $\gamma = 50$ and crystal fraction $\vartheta = 0.5$ unless specified otherwise.

4. Discussion

4.1. Comparison of Numerical Models to Linear Theory

In Michaut et al. (2013), a linearized dispersion relationship for magma gas porosity wave growth is presented. The full equations considered in Michaut et al. (2013) are identical to Equations 29–33 when $\mathrm{Da} \to \infty$, so $X_l = \mathcal{S}\rho_g^{1/2}$ and the transfer of volatile between phases is instantaneous. The model of Michaut et al. (2013) only considers basal oscillations in gas fraction, so $B = \phi$. The linear stability analysis conducted by Michaut et al. (2013) assumes zeroth order background states for ϕ, ρ_g, w_g, and w_m. These background states include a constant gas fraction, $\phi = \phi_0$, and magma velocity, $w_m = \mathcal{W}$ (see Appendix B for details).

The background gas density profile is imposed by the Darcy equation, (Equation 32), and equilibrated in Equation 31 (for $X_l = \mathcal{S}\rho_g^{1/2}$) by the time variation of the gas density (see Michaut et al. 2013, supplemental information and Appendix B). While the choice of this background state has been criticized by Hyman et al. (2019), our numerical results to the full nonlinear equations are in good agreement with the linear solutions of Michaut et al. (2013) and confirm their relevance. Particularly, neglecting the gas density gradient in the linear stability analysis by assuming a constant gas density of the background state (Hyman et al., 2019) points to highly localized unstable porosity waves with wavelengths of only several compaction lengths. Such waves should quickly decay by magma compaction as demonstrated by the results of the full numerical solution. This further demonstrates the importance of maintaining a strong gas density gradient to the generation and preferential selection of magma gas wave as a function of their wavelength.

The maximum instability $\max(q)$ of gas waves is compared to the stability analysis of Michaut et al. (2013), where C is wave amplitude growth rate versus frequency (Figure 8). We compare the maximum instability of the bottom 10%, 20%, 40%, and 80% of the domain to illustrate the increasing instability of gas waves with increasing z. Instability of gas waves is enhanced with increasing z because gas expands more readily with decreasing pressure. The stability analysis conducted by Michaut et al. (2013) assumes background states that reflect the basal properties of the conduit. However, all relevant numerical solutions show significant increases in gas fraction and magma velocity during ascent of magma. As expected, the maximum calculated instability, $\max(q)$, most resembles the analytical amplitude growth rate, C, near the base of the conduit where $\phi \approx \phi_0$ and $w_m \approx \mathcal{W}$.

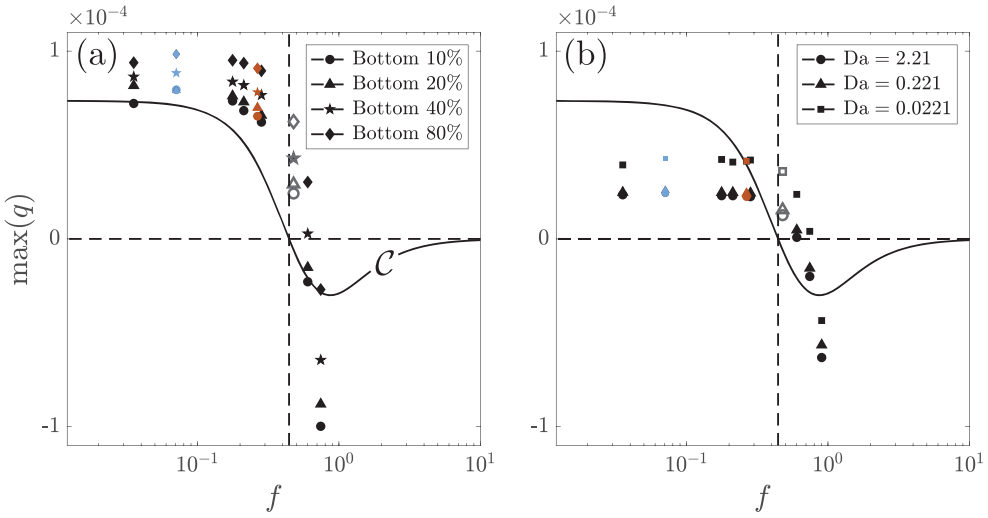

Figure 8. (a) Water-free comparison of maximum calculated instability max(q), to stability analysis of Michaut et al. (2013), where C is wave amplitude growth rate versus frequency. Maximum calculated instability is shown over four intervals to illustrate increasing instability with with dimensionless height, z, in the magma column. For example, the range $[z = 1, z = 0.1{\times}H/\delta_0]$ is used for calculating the max(q) profile for "bottom 10%." For a 5-km conduit and the material properties of Figure 4, $H \approx 113\delta_0$. The first compaction length is omitted from the interval used to calculate instantaneous growth rate to avoid boundary effects. (b) Comparison of max(q) including exsolution of water. Maximum growth is plotted above the inflection point on the steady-state profile for X_l (see section 4.2) and C when $B = \phi$ and a basal water content of $X_0 = S\rho_0^{1/2} = 0.0398$ are assumed. For convenience of comparison to Figures 6 and 7, the three frequencies $f = 0.0620$, $f = 0.2568$, and $f = 0.4692$ have been highlighted in Panels (a) and (b).

4.2. Corner Frequency and Gas Wave Growth

The frequency at which max(q) or $C = 0$ is similar to a "corner frequency" that defines the cut-off for a low-pass filter (i.e., which filters out modes with frequencies higher than the corner value). Above the corner frequency, perturbations to the steady state are attenuated by magma compaction. Perturbations at frequencies below the corner frequency are unstable and grow in amplitude as gas expands. For the case of water-free melt, $B = \phi$ and $X_0 = 0$ (Figure 8a), the corner frequency shifts slightly to the right, with increasing z thereby admitting higher frequency gas waves at shallower depths.

For cases where X_l and $X_0 \neq 0$, some additional considerations are required. When dissolved water is present, the magma-gas mixture may remain out of equilibrium during extraction. Depending on the Damköhler number, Da, the magma-gas mixture will be at different stages of degassing for a given depth z. For consistency, we compare max(q) above the curved portion on the steady-state profile for X_l (where $\partial X_l/\partial z$ approaches a constant slope, as in the upper portions of Figure 3d). Although the amount of water dissolved in the melts is different depending on Da, in this region, the compositional and viscosity gradients are roughly equal through the rest of the conduit and set by the power-law relationship between gas pressure and dissolved water content (see Figures 3c and 3d). Using the material properties and characteristic magma ascent rate from Figure 4 and the Damköhler numbers of Da = 2.21, Da = 0.221, and Da = 0.0221, we take max(q) above the dimensionless heights of $z = 0.6$, $z = 4.2$, and $z = 41.4$ (denoted by red dotted lines in Figures 7d–7f). Assuming a 5-km conduit and a characteristic compaction length of $\delta_0 = 44.4$ m, the height of the conduit is given by $H = \max(z) \approx 113$.

To test the sensitivity of the corner frequency and gas wave instability to dissolved water content, we first consider the case where $B = \phi$ at $z = 0$ in Equation 38c. We calculate max(q) for each frequency excited above the curved portion in the steady-state profile for X_l. Increasing Damköhler number demonstrates the sensitivity of gas wave instability to dissolved water and characteristic exsolution rate (Figure 8b). Moderately low-frequency modes are least stable and slightly higher frequency modes are admitted by the low-pass filter than predicted by Michaut et al. (2013). With increasing Da, gas wave instability becomes more suppressed across all modes. This generally flattens the pattern of max(q) when compared to the water-free simulations (Figure 8a). The corner frequency is not strongly affected by Damköhler number although increasing Da allows for a slightly less stringent low-pass filter (Figure 8b). However, for simulations when $B = \phi$, it

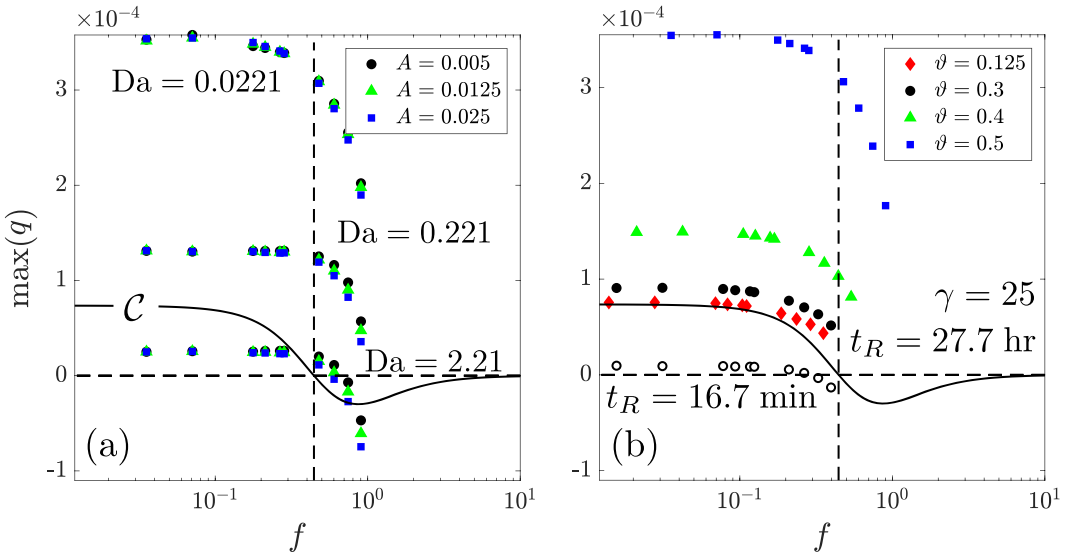

Figure 9. (a) Comparison of maximum calculated instability, max(q), to stability analysis of Michaut et al. (2013). The black line marked C is the wave amplitude growth versus frequency. Waves were excited by oscillating the dissolved water content of melt around the saturated value given by $X_0 = S\rho_0^{1/2} = 0.0398$. This plot illustrates that the calculated instability is sensitive to Damköhler number but not the amplitude, A, of perturbation in Equation 38c. The clustering of calculated max(q) for all amplitudes plotted here suggests that the imposed porosity wave perturbations are sufficiently small that they do not strongly excite nonlinear features of the governing equations. Therefore, the model results presented here are appropriate for comparison to previous linear stability analysis. In Panel (a), $\gamma = 50$. (b) Calculated instability max(q) as a function of crystal content ϑ, where the packing volume fraction of crystals $\vartheta_p = 0.6$. Waves were excited by the same manner as in Panel (a). Material properties of magma are the same as in previous Figure 4 with the exception of $\gamma = 25$. Similarities between top curves in Panels (a) and (b) illustrate that wave growth rate is insensitive to γ. The dimensional wavelength of each perturbation is the same across all simulations which causes the shift in dimensionless frequency. This is because the characteristic compaction length, δ_0, decreases with decreasing crystal content, ϑ. The compaction lengths are $\delta_0 = 17.3$ (red diamonds), $\delta_0 = 19.4$ (black circles), $\delta_0 = 26.3$ (green triangles), and $\delta_0 = 44.3$ (blue squares) m, respectively. For the constant characteristic degassing time scale $t_R = 27.7$ hr, the corresponding Damköhler numbers are Da = 0.0086, Da = 0.0097, Da = 0.0132, and Da = 0.0221 in order with increasing ϑ. The empty black circles show max(q) calculated with a much faster characteristic degassing time scale $t_R = 16.7$ min and $\vartheta = 0.3$.

is apparent that gas wave instability is dampened at a range of exsolution rates and resultant Damköhler numbers.

When oscillations in gas fraction are driven by changes in basal water content, ($B = X_l$ in Equation 38c), we show that the corner frequency and overall gas wave instability are quite sensitive to Damköhler number. This sensitivity of gas wave instability can be attributed to the characteristic reaction time scale for two primary reasons. First, fast degassing (i.e., high Damköhler number) suppresses the gas density gradient, which diminishes overall gas wave instability. Second, as exsolution time scales become slower, lower frequency modes interact by exchanging water between magma and the gas phase more effectively than high-frequency modes. Thus, we observe a far less stringent low-pass filter than predicted by Michaut et al. (2013) but with the relative amplification of low-frequency modes (Figure 9). Continuous exsolution throughout the conduit modifies the filter proposed by Michaut et al. (2013) so that gradual exsolution of gas from melt bolsters high-frequency modes against magma compaction. Nevertheless, low-frequency modes are fed by exsolution as well and experience significant expansion which results in much higher growth rates for long wavelength porosity waves.

Importantly, the growth rate for gas waves is unaffected in our simulations by the amplitude of oscillation, A in Equation 38c, for relevant values. This indicates that the oscillations imposed on the boundary for the full numerical solutions are small enough to be compared with the linearized dispersion relationship described in Appendix B. In the case where $A = 0.025$, with $X_0 = 3.98\%$, the superposition of 10 sinusoidal perturbations would result in oscillations between ~3 and 5 weight percent water dissolved in the melt. Significantly

smaller oscillations in dissolved water content are capable of exciting a range of gas porosity waves where low-frequency modes expand at rates much faster than their low-frequency counterparts (Figure 9).

4.3. Effect of Crystal Content on Gas Wave Growth

Variation of the crystal fraction, ϑ, has two primary effects on the results we present in this study. First, the compaction length (Equation 20) is reduced because the melt and crystal mixture is less viscous at lower crystal fractions (Equation 21). The shift in compaction length does not have a major impact on porosity wave growth alone. Second, at constant dissolved water content, the melt portion of the magma becomes comparatively water rich with decreasing crystal fraction.

As crystal fraction decreases, the balance between the mass transfer term, $\Gamma = \mathrm{Da}(X_l - \mathcal{S}\rho_g^n)$, and the left-hand side of the equation for conservation of mass of water, (Equation 31), results in faster degassing. This further accentuates the tendency of water dissolved in the melt to reduce gas decompression across the magma column and thus dampen oscillations. With increasing Damköhler number, simulations with low magma crystal content show a shift in the corner frequency toward low frequencies, meaning the low-pass filter for porosity waves becomes more strict (Figure 9b). However, the growth of porosity waves that do pass through the filter is exceedingly small and similar for a wide range of frequencies. Therefore, a narrow frequency range comparable to data from Figure 1 is unlikely to occur unless there is a significant crystal fraction and degassing in the conduit proceeds slowly (Figure 9b).

The simulations in this manuscript treat the crystal fraction, ϑ, as constant throughout the magma column during ascent. A recent numerical model for decompression-induced crystallization of Pinatubo magma (Befus & Andrews, 2018) suggests that magma decompressing at a rate of 3–4 MPa hr^{-1} result in $\ll$10% crystallization by volume of plagioclase microlites. Although other phases such as amphibole and clinopyroxene will crystallize, we consider their effect to be negligible for our model at the decompression rates examined in this study. However, if significant crystallization was to occur, we expect it to enhance the growth of porosity gas waves with low frequencies disproportionately. Figure 9b shows magma with $\vartheta = 0.125$, $\vartheta = 0.3$, $\vartheta = 0.4$, and $\vartheta = 0.5$. If magma was with initial crystal fraction of $\vartheta = 0.3$ to gain $\sim$20% crystals by volume, the calculated growth rate quadruples for low-frequency modes that pass the filter. The growth rate for moderately high-frequency modes that pass the filter only doubles, further biasing the power of the signal to longer wavelength features. As such, crystallization during degassing enhances gas wave growth, for low-frequency perturbations especially in cases where Damköhler number is low. Nevertheless, degassed, highly crystalline magma is more conducive to long period oscillations than crystal poor, water oversaturated magma. This suggests that the mode of magma mixing and degassing within the chamber must produce a crystal-rich magma to support growing porosity waves of magmatic gas.

4.4. Porosity Wave Ascent Time

For the majority of examples presented in this study (Figures 3–9), Damköhler numbers are calculated assuming a characteristic magma velocity of $\mathcal{W} = 0.02$ m s^{-1}, crystal fraction $\vartheta = 0.5$ a reference compaction length of $\delta_0 = 44.4$ m, and a characteristic exsolution time scale, t_R, that ranges from minutes to days. When Da = 2.21, Da = 0.221, and Da = 0.0221, the characteristic exsolution time scale, t_R, is 16.7 min, 2.67 hr, and 27.7 hr, respectively. Numerical simulations show that additional frequencies are not excited by the small perturbations used to conduct this study (Figures 5 and 9) and that $w_g \approx w_m$ due to the large drag between phases (dimensionless $\Delta w \ll 1$ in Equations 32 and 33). Therefore, both phases of the mixture travel together with porosity wave frequencies locked in place although wave amplitudes may grow or decay. Using the steady-state profiles for magma and gas velocity generated in Figure 3, we find that the travel time for a parcel of the magma gas mixture to traverse the 5-km column is about 45 hr. With these considerations, we explore scenarios that are the most and the least likely to produce long period oscillations (Figure 1) given a combination of Damköhler number and perturbation type.

When reaction rates are very fast compared to the conduit residency time, the gas wave instability, max(q), predicted by Michaut et al. (2013), is suppressed (Figures 8b and 9). For example, when Da $\sim$ 1, equilibrium where $X_l = \mathcal{S}\rho_g^n$ is reached quickly and the gas wave selection due to the competition between gas expansion and magma compaction described by Michaut et al. (2013) ensues with two additional caveats: (1) Fast exsolution diminishes the gas density (and therefore gas pressure gradient) which lessens the gas wave instability, and (2) moderately high-frequency modes near the predicted corner frequency are bolstered against magma compaction by continued exsolution throughout the conduit. These new considerations act to minimize the

mechanical filtering effect proposed in Michaut et al. (2013) by reducing the instability of low-frequency modes and increasing the instability of moderately high-frequency modes. In particular, models including exsolution where $B = \phi$ display less overall gas wave instability in conjunction with less filtering than their water-free counterparts (Figures 8a and 8b).

In several models presented here, Da = 0.0221, which corresponds to a characteristic exsolution time scale that is half of the residency time of the magma gas mixture in the conduit. With this slow characteristic exsolution time scale, values of max(q) are systematically shifted upward indicating greater porosity wave growth in the column for either type of boundary condition in Equation 38c. Furthermore, perturbations in X_l result in extremely amplified growth of porosity waves at low frequency compared to high frequency. Therefore, in a case where $B = X_l$, sluggish exsolution, or low Damköhler number, does not precisely act as a low-pass filter for porosity waves as proposed by Michaut et al. (2013). However, the biased amplification of low-frequency modes effectively concentrates the power of wavelike perturbations in long wavelength porosity waves.

Oscillations form the wavelike perturbations at the bottom boundary where $w_m = \mathcal{W} = 0.02\,\mathrm{m\,s^{-1}}$. After redimensionalizing frequency, the wavelength for the sinusoidal perturbations is used as a test case in this study, $\lambda = \mathcal{W}/f$ (sections 2.5–4.2 and figures therein) rangees from $\lambda = 1{,}667$ m to $\lambda = 49.5$ m. The wavelength of modes highlighted in light blue, orange, and gray in Figures 6–8 have wavelengths of $\lambda = 741.2$ m, $\lambda = 172.4$ m and $\lambda = 94.3$ m. Numerical simulations show that the residency time of a gas wave in a 5-km conduit is about 45 hr. The average vertical velocity of the magma gas mixture in the column is then $\bar{w} = 0.031\,\mathrm{m\,s^{-1}}$. Thus, the average time between porosity wave peaks with wavelength λ arriving from depth to the shallow conduit is $\bar{t} = \lambda/\bar{w}$. For the superposition of 10 sinusoidal perturbations tested numerically in this study, the average arrival frequency of waves ranges from $\bar{t} \sim 27$ min to 15 hr.

Comparing the results of our numerical analysis to the observations of Mori et al. (1996), Voight et al. (1999), and Wylie et al. (1999) (summarized in Figures 1a and 1b), we find that the amplification of porosity waves as a mechanism for producing long period eruptive precursors at silicic volcanoes is most likely if the waves are formed due to small perturbations in dissolved water content of the melt. Model results where $B = \phi$ with $X_0 = 0.0398$ show the filtering effect owing to magma compaction is minimized and the overall gas instability is too little to produce the main trend of the long period oscillations observed at Pinnatubo and Soufrière Hills. However, when $B = X_l$, we observe a significant amplification of porosity waves with decreasing Damköhler number. When Da ~ 1, high-frequency modes are not admitted by the column but the gas wave instability is small. When Da < 1, porosity waves with wavelengths corresponding to periodic arrival times of ~10 hr grow two to four times faster than those that arrive on hourly time scales (Figure 9).

4.5. Implications for Long Period Oscillations at Silicic Volcanoes and Their Magmatic Systems

In this manuscript, we present a conceptual model to examine the viability of porosity waves with compressible gas as a potential mechanism for exciting long period volcanic oscillations. Our theoretical model suggests that porosity waves with periods 10 hr or longer are amplified if the waves are excited by gradual degassing during magma ascent. The mechanism for inducing long period oscillations examined in this manuscript requires small temporal variation in magma water saturation at the base of the conduit. The basal variation in the dissolved water content of magma reflects heterogeneity in composition or temperature within the magma chamber. Therefore, the theoretical model implies that magma chamber heterogeneity and mixing are conducive to conditions where porosity waves may arise with a distinct temporal pattern (as observed in RSAM the data showin in Figure 1).

Recent modeling studies suggest that rapid mixing of magma may lead to long-lived magma chamber heterogeneity even without addition of new batches of magma (Garg et al., 2019). Additionally, petrological evidence suggests that parts of the magma chamber were at much higher temperatures than the inferred average at Soufrière Hills Volcano. Couch et al. (2001) invoke self-mixing in the form of Rayleigh-Bénard convection to explain the apparent co-location of minerals that cannot coexist under equilibrium conditions. Other petrological studies detail evidence for periodic magma heating and remobilization within the magma chamber (Zellmer et al., 2003). Furthermore, the combination of magma heterogeneity and the temperature sensitivity for the diffusivity of water (Baker et al., 2005, and references therein) may result in uneven degassing and variation in water saturation for magma exiting the magma chamber. Any combination of the aforementioned mechanisms could account for the variation in dissolved water content in magma at the base of our proposed model. The numerical results show that porosity wave filtering is largely unaffected

by the amplitude of perturbations (Figure 9) and biased porosity wave growth is expected to arise from very small basal variations in either gas fraction or volatile content of the magma.

The onset of long period oscillations leading up to elevated volcanic activity may indicate the heating, remobilization, and mixing of magma. This could take the form of either self-mixing or magma chamber replenishment. At Soufrière Hills, andesite phenocrysts that erupted between December 1995 and August 1997 have a range of textures and zonation patterns that suggest that nonuniform reheating of the magma occurred directly before the onset of the major eruption (Murphy et al., 1998). The nonuniform reheating is interpreted by Murphy et al. (1998) as remobilization of the resident magma which lead to self-mixing and may have eventually triggered the eruption at Soufrière Hills. The onset of regular periodic precursors may be a near real-time indicator that magma chamber mixing has begun. Initially, random heterogeneity could result in an apparent pattern where magma chamber mixing signatures of selected wavelengths are expressed at the surface due to the accentuation of moderately long porosity waves.

At Pinatubo in 1991, periodic oscillations were attributed to gas vesiculation following a climactic eruption (Mori et al., 1996). Directly following the eruption the conduit was unimpeded allowing open system degassing. As the vent cooled, waning effusive eruption continued, and seismic activity decayed in an exponential fashion. Mori et al. (1996) hypothesize that conduit gradually began to seal itself. However, this process was not uniform allowing small portions of the volcanic plumbing to become overpressured, resulting in small explosions linked with the long period oscillations. Within our conceptual model, decompressing magma with varying dissolved water and crystal content could cool enough and reach a threshold where there is sufficient crystal content to support the growth of porosity waves. Once this threshold is reached, small variations in water could result in porosity waves of preferred wavelength and account for the regularity of the small explosions discussed by Mori et al. (1996). Further study would be required to link potential heterogeneity in melt water content with the underlying magma chamber. Alternatively, the cyclicity observed at Pinatubo in 1991 could be a consequence of transitioning from open-system degassing—after explosion—to quasi-open system degassing—after reestablishment of a cohesive magma column. At the very least, similar magma ascent rates at Pinatubo and Soufrière Hills ($\sim$0.01–0.06 m s^{-1}; Cassidy et al., 2018), and the corresponding regular periodicity of 7–10 hr for elevated volcanic activity at both volcanoes is curious and warrants future comparative study.

5. Summary and Conclusion

In this study, we constructed a theoretical model with the goal of understanding how volatile degassing and local variations in magma viscosity within a volcanic conduit may affect long period oscillations, such as those observed at Pinatubo and Soufrière Hills. To this end, we compare two end-member models where very small oscillations induce magmatic gas porosity waves:

1. Oscillations are due to small changes in gas fraction entering the conduit.
2. Oscillations are due to small changes in water content of melt at the base of the conduit.

When gas waves are generated by small changes in gas fraction entering the conduit, we find that the addition of dissolved water in melt dampens gas wave expansion. This reduces the efficacy of the mechanical gas wave selection model proposed by Michaut et al. (2013). Models additionally show that local viscosity changes have only a small effect on wave stability. Despite our choice to use a simplified expression for magma viscosity, (Equation 12), melt viscosity varies by more than two orders of magnitude in numerical models. Model results with large spatial and temporal changes in magma viscosity reveal that maintaining a large gas density gradient in the magma column is the most important factor for inducing gas wave instability.

When waves are generated by small changes in melt water content entering the base of the conduit, we infer a separate mechanism for selecting gas waves that can also contribute to the isolation of long period oscillations. Petrological observations suggest that the magma source beneath Soufrière Hills Volcano was reheated or remixed at the time when long period oscillations began in 1997, thus providing a possible mechanism for changes in melt water content (Murphy et al., 1998). Further study is required to make the same claim for Pinatubo postclimactic eruption in 1991. The rate of degassing, described by the dimensionless Damköhler number, affects wave growth throughout the column. When reaction rates are fast, Da $\sim$ 1, high-frequency modes are filtered away but gas wave instability is small. When Da $<$ 1, porosity waves with wavelengths

long enough to induce long period oscillations such as those observed at Pinatubo and Soufrière Hills grow two to four times faster than higher frequency modes.

We conclude that gradual degassing in the volcanic conduit during ascent of magma is favorable for the preferential growth of low-frequency magma gas waves. Slower degassing naturally interacts with the magma column on longer wavelength scales, promoting the growth of lower frequency waves. The resulting pattern of wave growth, biased toward the waves with arrival times of several hours or more at the surface, is commensurate with the periodicity of cyclical degassing, dome-growth, and ground deformation observed at Pinatubo and Soufrière Hills Volcano (Mori et al., 1996; Voight et al., 1999; Watson et al., 2000; Wylie et al., 1999). Short time scale magma chamber mixing provides a viable mechanism for heterogeneity in melt water content required to produce long wavelength magma gas porosity waves. The similarity of periodicity at Pinatubo and Soufrière Hills Volcano hints that there is a common mechanistic source for the phenomenon at both volcanoes. We demonstrate that degassed, crystal-rich magma is more conducive to the growth of gas waves that may result in the periodic behavior and suggest that porosity waves induced by gradual degassing are a viable candidate for that periodic behavior. Porosity waves are a ubiquitous feature in poroviscous materials and may be linked with cyclical episodes of elevated volcanic activity observed elsewhere.

Appendix A: Discrete Growth of Magma Gas Waves

Consider a linear function, $\chi(z,t)$, that varies with a spatial coordinate and time. A Fourier series for the function may be written

$$\chi(z,t) = \sum_{j=1}^{N} \hat{\chi}_j(z) \cos\left(\omega_j t - k_j z\right), \tag{A1}$$

where ω_j is the jth angular frequency of a sinusoidal perturbation prescribed at the boundary, $z = 0$, and the angular wavenumber is given by k_j. We assume the relation

$$\chi_j = \mathcal{B} e^{\mathcal{C}_j z}, \tag{A2}$$

where $\mathcal{C}_j$ is the growth rate of the jth perturbation with the vertical coordinate z and $\mathcal{B}$ is a constant. We define

$$A_j = \frac{1}{2}\hat{\chi}_j(z)\left(\cos(k_j z) - i\sin(k_j z)\right). \tag{A3}$$

The power of the signal, χ, at the jth frequency is

$$\mathcal{P}_j = A_j A_j^* = \frac{1}{4}\hat{\chi}_j^2(z), \tag{A4}$$

where A_j^* is the complex conjugate of A_j.

The growth rate across all excited frequencies are found by differentiating $\mathcal{P}$ along the spatial coordinate so

$$\mathcal{C}_j(z) = \frac{1}{2\mathcal{P}_j}\left(\frac{\mathrm{d}\mathcal{P}_j}{\mathrm{d}z}\right). \tag{A5}$$

Additionally, the phase shift and wave number of $\chi(z,t)$ can be found using the imaginary and real parts of A_j

$$S_j = \tan(k_j z) = \frac{-\mathrm{Im}(A_j)}{\mathrm{Re}(A_j)}, \tag{A6}$$

and

$$k_j = \frac{1}{z}\tan^{-1}\left(\frac{-\mathrm{Im}(A_j)}{\mathrm{Re}(A_j)}\right). \tag{A7}$$

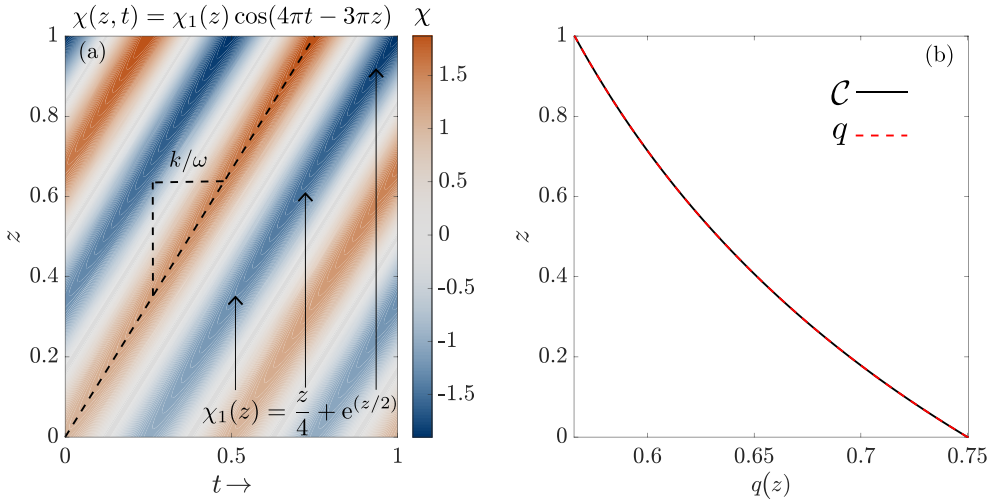

Figure A1. Simple benchmark calculation for a periodic function of a single frequency $\chi(z,t) = \chi_1\cos(\omega t - kz)$ where growth rate varies as a function of z. In this example, $\omega = 4\pi$ and $k = 3\pi$. (a) Demonstration of evolution of $\chi(z,t)$ over N time samples in the interval $t \in [0, (1-\Delta t)]$ for each of the n_z grid points in a model domain. Black dashed line shows the numerical calculation for signal shift. The shift of the signal is prescribed by wavenumber k and the angular frequency ω at the bottom boundary. Note two full cycles in χ throughout the model domain indicating that linear frequency, $f = 2$, is equal to two. (b) Black line: analytical growth rate derived from inserting $\chi_\omega(z)$ into Equation A5. Red dashed line: approximate growth rate calculated using the solution grid from (a).

To relate numerical model output to the linear growth rate, the model output is treated as a time series sampled at n_t evenly spaced time steps. A Fourier transform is used on $\chi(z,t)$ to obtain $\hat{\chi}(z,\omega)$. The numerical power of χ at a given depth is

$$\Pi_j(z,\omega_j) = \hat{\chi}_j\hat{\chi}_j^*, \tag{A8}$$

for the jth frequency of a sinusoidal perturbation prescribed at the boundary, $z = 0$. Equation A8 is the numerical analogue to Equation A4. The power of the signal Π for each frequency is calculated at each grid-block z, which results in n_z power spectra for each frequency. The numerical growth or decay of the signal, q_j, is found by differencing Π_j throughout the model grid to obtain an approximation for the gradient of the power with depth. Once $(d\mathcal{P}/dz)$ is approximated using Π, numerical growth may be constructed using $q \approx \mathcal{C}$. The phase shift and wavenumber for a given frequency may also be obtained numerically by using $\hat{\chi}_j$ and its complex conjugate. Figure A1 shows a linear benchmark calculation demonstrating the recovery of model growth rate for a single frequency.

Appendix B: Linearized Dispersion Relationship

We compare numerical solutions of Equations 29–33 with a dispersion relationship for simplified, linearized governing equations. We use the dispersion relationship to obtain a growth rate for gas waves, $\mathcal{C}$, as a function of frequency. For the linear stability analysis presented in section 4, we assume isoviscous, water-free magma and a Darcian drag coefficient. Using the characteristic scales presented in section 2.3, the dimensionless governing equations are

$$\frac{\partial(1-\phi)}{\partial t} + \frac{\partial}{\partial z}\left[(1-\phi)w_m\right] = 0, \tag{B1}$$

$$\frac{\partial\phi\rho_g}{\partial t} + \frac{\partial}{\partial z}\left[\phi\rho_g w_g\right] = 0, \tag{B2}$$

$$-\beta\frac{\partial\rho_g}{\partial z} - \rho_g + \frac{\alpha}{\phi}\Delta w = 0, \tag{B3}$$

$$\alpha\frac{\partial}{\partial z}\left[\left(\frac{1-\phi^2}{\phi}\right)\frac{\partial w_m}{\partial z}\right] - (1-\phi)(1-\rho_g) - \frac{\alpha}{\phi}\Delta w = 0. \tag{B4}$$

where

$$\alpha = \frac{\mathcal{W}\mu_g}{k_0\rho_m g}, \tag{B5a}$$

$$\beta = \frac{C_g^2}{g\delta_0}, \tag{B5b}$$

and

$$\delta_0 = \sqrt{\frac{4}{3}\frac{\mu_m k_0}{\mu_g}}, \tag{B6}$$

for $\mathcal{G} = 4/3$ (Table 1).

The zeroth order background state for Equations B1–B4 are given in Michaut et al. (2013) as

$$\phi^{(0)} = \phi_0, \tag{B7}$$

$$w_m^{(0)} = 1, \tag{B8}$$

$$\rho_g^{(0)} = \rho_0 + \frac{\partial \rho_g^{(0)}}{\partial z}z + \frac{\partial \rho_g^{(0)}}{\partial t}t, \tag{B9}$$

$$w_g^{(0)} = 1 + \frac{\phi_0(1-\phi_0)(1-\rho_0)}{\alpha} - \frac{\phi_0(1-\phi_0)}{\alpha}\left(\frac{\partial \rho_g^{(0)}}{\partial z}z + \frac{\partial \rho_g^{(0)}}{\partial t}t\right). \tag{B10}$$

For details describing the derivation of zeroth order equations, see Michaut et al. (2013) supplementary materials. Next, we assume small wavelike perturbations in gas fraction, gas density along with magma and gas velocity of the magma, so

$$\phi = \phi_0 + \epsilon\phi^{(1)}e^{i(kz-\omega t)}, \tag{B11}$$

$$\rho_g = \rho_g^{(0)} + \epsilon\rho_g^{(1)}e^{i(kz-\omega t)}, \tag{B12}$$

$$w_g = w_g^{(0)} + \epsilon w_g^{(1)}e^{i(kz-\omega t)}, \tag{B13}$$

$$w_m = 1 + \epsilon w_m^{(1)}e^{i(kz-\omega t)}. \tag{B14}$$

Here, the superscript (1) indicates a perturbation to the governing equations, ω is the angular frequency of the perturbation, k is the wave number of the perturbation, and the constant $\epsilon \ll 1$. Inserting Equations B11–B14 and B7–B10 into the governing Equations B1–B4, we write expressions for the first-order perturbations in ϵ

$$(\omega - k)\phi^{(1)} + k(1-\phi_0)w_m^{(1)} = 0, \tag{B15}$$

$$\begin{aligned}&\phi_0\left[2\frac{\phi_0(1-\phi_0)(1-\phi_0+\phi_0\rho_0)}{\alpha\beta} + i\left(k-\omega+\frac{k(1-2\rho_0)\phi_0(1-\phi_0)}{\alpha}\right)\right]\rho_g^{(1)}\\ &+i\rho_0\left(k-w+\frac{k\phi_0(1-\phi_0)(1-\rho_0)}{\alpha}\right)\phi^{(1)} - \phi_0\left(\frac{1-\phi_0+\phi_0\rho_0}{\beta} - i\rho_0 k\right)w_g^{(1)} = 0,\end{aligned} \tag{B16}$$

$$(1-\rho_0)(1-\phi_0)\phi^{(1)} - \phi_0(ik\beta+\phi_0)\rho_g^{(1)} + \alpha(w_m^{(1)} - w_g^{(1)}) = 0, \tag{B17}$$

$$(1-\rho_0)(2\phi_0-1)\phi^{(1)} - \alpha\left[(1+k^2(1-\phi_0^2))w_m^{(1)} - w_g^{(1)}\right] = 0. \tag{B18}$$

This linear system of equations may be written in matrix form, $\mathbf{Mx} = \mathbf{0}$, where $\mathbf{x} = (\phi^{(1)}, \rho_g^{(1)}, w_g^{(1)}, w_m^{(1)})$. The characteristic polynomial of this system of linear equations leads to a dispersion relation for $\omega = 2\pi f$ as a

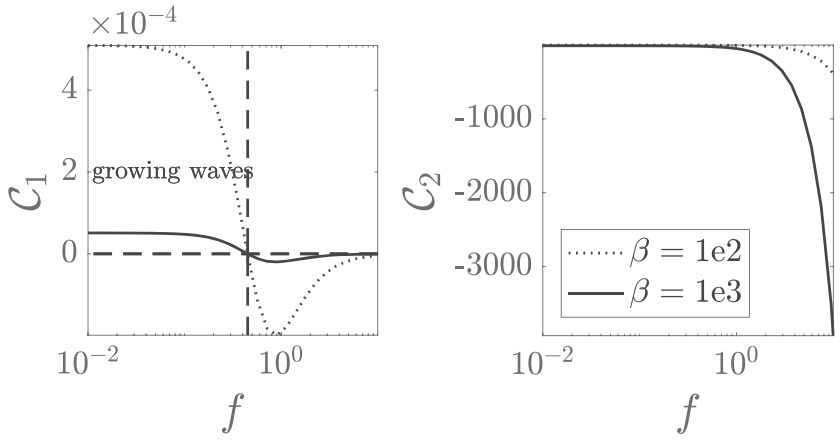

Figure B1. The two solutions to the dispersion relationship found by obtaining the characteristic polynomial of the linear system of Equations B15–B18.

function of wavenumber $k = 2\pi/\lambda$ (where λ is linear wavelength and f is frequency). We provide a short MATLAB script for symbolically solving this dispersion relationship (see Acknowledgements). The curve C in Figures 8 and 9 is obtained from

$$C_j = \frac{\mathrm{Im}(\omega_j)}{\mathrm{Re}(\omega_j)/k}. \tag{B19}$$

The second degree dispersion relationship has two solutions ($j \in [1, 2]$). However, we find that the first root is dominant for frequencies where waves grow and plot solutions for C_1 in section 4 and drop the subscript. The lowest negative values at high frequency in Figures 8 and 9 are likely affected by C_2 (Figure B1).

Appendix C: Boundary Conditions and Linearization of Steady-State Equations at $z = 0$

The initial and boundary conditions for the numerical solutions are selected based on simplified, linearized solutions to the governing equations. We assume that the source magma chamber beneath the bottom boundary (i.e., $z < 0$) has not begun to degas and had time to compact to an equilibrium gas fraction, ϕ_0. Upon entering the conduit (i.e., $z \geq 0$), compaction adjusts to changes in gas fraction caused by magma degassing and gas expansion during ascent and decompression. Under these assumptions, it is natural to assume that magma compaction is small ($\partial w_m/\partial z \approx 0$) at the conduit inlet. Classical one-dimensional models using similar theory for melt migration generally assume an arbitrary and hence unequilibrated fluid fraction at the bottom boundary (see McKenzie, 1984; Ribe, 1985). In such a case, compaction occurs abruptly after injection above $z = 0$, toward the equilibrium ϕ, forming a compacting boundary layer, in which case the assumption that $\partial w_m/\partial z$ is very small would not be applicable.

To demonstrate that $\partial w_m/\partial z \approx 0$ near $z = 0$, we linearize the dimensionless governing equations. Following Michaut et al. (2013), we assume that $\phi_0 \ll 1$ and $S \ll 1$. We also assume that the initial dimensionless gas density is much less than the magma $\rho_0 \ll 1$. We neglect the effect of crystal fraction and assume equilibrium ($X_l = S\rho_g^n$) for the steady-state solution near the base of the column. Additionally, we assume Darcian drag and that the exponent governing the gas-pressure dependence of water solubility is $n = 1/2$. The steady-state solutions are assumed to be linear with the vertical coordinate, z, and thus take the form

$$\phi \approx \phi_0 + a(1 - \phi_0)z, \tag{C1}$$

$$\rho_g \approx \rho_0 + bz, \tag{C2}$$

$$w_m \approx 1 + cz, \tag{C3}$$

$$w_g \approx \left(1 + \frac{\phi_0(1 - \phi_0)(1 - \rho_0)}{\alpha}\right)(1 + dz), \tag{C4}$$

where a, b, c, and d are constant coefficients (not to be confused with the Einstein or drag coefficients). The leading factor in Equation C4 is the initial gas velocity, $w_{g,0}$, described by Equation 37 in section 2.4. This quantity is obtained by assuming no compaction in Equation 33. At steady state, the dimensionless governing equations, (Equations 29–32), are recast as

$$\frac{\partial}{\partial z}\left[(1-\phi)\left(1-\mathcal{S}\rho_g^{1/2}\right)w_m\right]=0, \tag{C5}$$

$$\frac{\partial}{\partial z}\left[\phi\rho_g w_g+(1-\phi)w_m\right]=0, \tag{C6}$$

$$-\phi\beta\frac{\partial\rho_g}{\partial z}-\phi\rho_g+\alpha\Delta w=0. \tag{C7}$$

Here, Equation C5 is obtained by taking the difference between Equations 29 and 31 and neglecting the effects of crystal fraction (dropping the $(1-\vartheta)$ factor). Equation C6 arises from the sum of Equations 29 and 30. Lastly, Equation C7 is Equation 32 assuming Darcian drag so that $\mathcal{F}_j(\phi)=\phi$ in Equation 35. Employing Stokes drag, $\mathcal{F}_j(\phi)=\phi^{2/3}$, in Equation C7 makes separation between the magma and gas phases more difficult but does not alter our assumption that compaction will be small near $z=0$ for relevant model cases.

Equations C1–C4 are inserted into Equations C5–C7 yielding three equations that are zeroth order in z,

$$0=c\left(1-\phi_0\right)\left(1-\mathcal{S}\rho_0^{1/2}\right)-a\left(1-\phi_0\right)\left(1-\mathcal{S}\rho_0^{1/2}\right)-b\frac{\mathcal{S}\left(1-\phi_0\right)}{2\rho_0^{1/2}}, \tag{C8}$$

$$0=c(1-\phi_0)-a(1-\phi_0)+\left(a(1-\phi_0)\rho_0+b\phi_0+d\phi_0\rho_0\right)\left(\frac{\phi_0\left(1-\phi_0\right)\left(1-\rho_0\right)}{\alpha}+1\right), \tag{C9}$$

$$0=\rho_0+\left(1-\phi_0\right)\left(1-\rho_0\right)+b\beta, \tag{C10}$$

and one equation that is first order in z associated with Equation C7, given by

$$0=\alpha\left(c-d\left(\frac{\phi_0\left(1-\phi_0\right)\left(1-\rho_0\right)}{\alpha}+1\right)\right)-b\phi_0-a\rho_0\left(1-\phi_0\right)-ab\beta\left(1-\phi_0\right). \tag{C11}$$

Equations C8–C11 can be used to solve for the constant coefficients a, b, c, and d. We assume that the dimensionless number comparing characteristic magma ascent rate to characteristic gas segregation is greater than one, $\alpha\geq 1$. Assuming small $\mathcal{S}$ that the density of gas is much less than magma and low initial gas fraction (i.e., $(1-\mathcal{S}\rho_0^{1/2})\approx 1$, $(1-\rho_0)\approx 1$, and $(1-\phi_0)\approx 1$), the coefficients are

$$a\approx\left(\frac{1}{\beta\rho_0}\right)\left(\frac{\mathcal{S}}{2\rho_0^{1/2}}+\phi_0\right), \tag{C12}$$

$$b\approx-\frac{1}{\beta}, \tag{C13}$$

$$c\approx a, \tag{C14}$$

$$d\approx a\left(\frac{1+\alpha}{\alpha}\right). \tag{C15}$$

For the range of parameters relevant to this study (Table 1), the coefficients a, b, c, and d are small ($\sim 10^{-3}$ or less). In all numerical experiments explored in this manuscript, we set $\partial w_m/\partial z=0$ based on the observation that $c\ll 1$.

Data Availability Statement

The MATLAB code for computing the results and generating all figures can be found at https://zenodo.org/record/3910768#.XvaVpZNKg5s.

Acknowledgments
J. S. J. and D. B. were supported by NSF grant EAR-1645057. C. M. has received financial support of the IDEXLyon Project of the University of Lyon in the frame of the Programme Investissements dAvenir (ANR-16-IDEX-0005). The authors would like to acknowledge helpful reviews by Benjamin Andrews, Álvaro Aravena, and an anonymous reviewer which significantly improved the quality of this manuscript.

References

Aiuppa, A., Bitetto, M., Francofonte, V., Velasquez, G., Parra, C. B., Giudice, G., et al. (2017). A CO_2-gas precursor to the March 2015 Villarrica volcano eruption. *Geochemistry, Geophysics, Geosystems*, *18*, 2120–2132. https://doi.org/10.1002/2017GC006892

Anderson, K., Lisowski, M., & Segall, P. (2010). Cyclic ground tilt associated with the 2004–2008 eruption of Mount St. Helens. *Journal of Geophysical Research*, *115*, B11201. https://doi.org/10.1029/2009JB007102

Andrews, B. J., & Befus, K. S. (2020). Supersaturation nucleation and growth of plagioclase: A numerical model of decompression-induced crystallization. *Contributions to Mineralogy and Petrology*, *175*(3), 1–20.

Aravena, A., & Vitturi, M. d. M. (2018). Mamma (magma ascent mathematical modeling and analysis). https://vhub.org/resources/mamma

Aravena, A., Vitturi, M. d., Cioni, R., & Neri, A. (2017). Stability of volcanic conduits during explosive eruptions. *Journal of Volcanology and Geothermal Research*, *339*, 52–62.

Bagdassarov, N., Dingwell, D. B., & Wilding, M. (1996). Rhyolite magma degassing: An experimental study of melt vesiculation. *Bulletin of volcanology*, *57*(8), 587–601.

Baker, D. R., Freda, C., Brooker, R. A., & Scarlato, P. (2005). Volatile diffusion in silicate melts and its effects on melt inclusions. *Annals of Geophysics*, *48*(4–5), 699–717.

Barmin, A., Melnik, O., & Sparks, R. (2002). Periodic behavior in lava dome eruptions. *Earth and Planetary Science Letters*, *199*(1–2), 173–184.

Batchelor, C. K., & Batchelor, G. (2000). *An introduction to fluid dynamics*. Cambridge, UK: Cambridge University Press.

Befus, K. S., & Andrews, B. J. (2018). Crystal nucleation and growth produced by continuous decompression of Pinatubo magma. *Contributions to Mineralogy and Petrology*, *173*(11), 92

Bercovici, D., & Michaut, C. (2010). Two-phase dynamics of volcanic eruptions: Compaction, compression and the conditions for choking. *Geophysical Journal International*, *182*(2), 843–864.

Bercovici, D., & Ricard, Y. (2003). Energetics of a two-phase model of lithospheric damage, shear localization and plate-boundary formation. *Geophysical Journal International*, *152*(3), 581–596.

Burnham, C. W., & Davis, N. (1974). The role of H_2O in silicate melts; II, Thermodynamic and phase relations in the system NaAlSi3O 8-H_2O to 10 kilobars, 700 degrees to 1100 degrees C. *American Journal of Science*, *274*(8), 902–940.

Burton, M., Mader, H., & Polacci, M. (2007). The role of gas percolation in quiescent degassing of persistently active basaltic volcanoes. *Earth and Planetary Science Letters*, *264*(1–2), 46–60.

Caricchi, L., Annen, C., Blundy, J., Simpson, G., & Pinel, V. (2014). Frequency and magnitude of volcanic eruptions controlled by magma injection and buoyancy. *Nature Geoscience*, *7*(2), 126–130.

Caricchi, L., & Blundy, J. (2015). The temporal evolution of chemical and physical properties of magmatic systems. *Geological Society, London, Special Publications*, *422*(1), 1–15.

Cashman, K. V., Sparks, R. S. J., & Blundy, J. D. (2017). Vertically extensive and unstable magmatic systems: A unified view of igneous processes. *Science*, *355*(6331), eaag3055.

Cassidy, M., Manga, M., Cashman, K., & Bachmann, O. (2018). Controls on explosive-effusive volcanic eruption styles. *Nature Communications*, *9*(1), 2839.

Costa, A. (2005). Viscosity of high crystal content melts: Dependence on solid fraction. *Geophysical Research Letters*, *32*, L22308. https://doi.org/10.1029/2005GL024303

Couch, S., Sparks, R., & Carroll, M. (2001). Mineral disequilibrium in lavas explained by convective self-mixing in open magma chambers. *Nature*, *411*(6841), 1037–1039.

Denlinger, R. P., & Hoblitt, R. P. (1999). Cyclic eruptive behavior of silicic volcanoes. *Geology*, *27*(5), 459–462.

Eichelberger, J. C. (1995). Silicic volcanism: Ascent of viscous magmas from crustal reservoirs. *Annual Review of Earth and Planetary Sciences*, *23*(1), 41–63.

Eichelberger, J. C., Carrigan, C. R., Westrich, H. R., & Price, R. H. (1986). Non-explosive silicic volcanism. *Nature*, *323*(6089), 598.

Fowler, A. (1985). A mathematical model of magma transport in the asthenosphere. *Geophysical & Astrophysical Fluid Dynamics*, *33*(1–4), 63–96.

Gardner, J. (2009). The impact of pre-existing gas on the ascent of explosively erupted magma. *Bulletin of Volcanology*, *71*(8), 835–844.

Gardner, J., Rutherford, M., Carey, S., & Sigurdsson, H. (1995). Experimental constraints on pre-eruptive water contents and changing magma storage prior to explosive eruptions of Mount St Helens volcano. *Bulletin of Volcanology*, *57*(1), 1–17.

Garg, D., Papale, P., Colucci, S., & Longo, A. (2019). Long-lived compositional heterogeneities in magma chambers, and implications for volcanic hazard. *Scientific Reports*, *9*(1), 1–13.

Giordano, D., Russell, J. K., & Dingwell, D. B. (2008). Viscosity of magmatic liquids: A model. *Earth and Planetary Science Letters*, *271*(1-4), 123–134.

Girina, O. A. (2013). Chronology of Bezymianny Volcano activity, 1956–2010. *Journal of Volcanology and Geothermal Research*, *263*, 22–41.

Gonnermann, H. M., & Manga, M. (2007). The fluid mechanics inside a volcano. *Annual Review of Fluid Mechanics*, *39*, 321–356.

Hammer, J. E., & Rutherford, M. J. (2002). An experimental study of the kinetics of decompression-induced crystallization in silicic melt. *Journal of Geophysical Research*, *107*(B1), ECV 8-1-ECV 8-24. https://doi.org/10.1029/2001JB000281

Hess, K., & Dingwell, D. (1996). Viscosities of hydrous leucogranitic melts: A non-Arrhenian model. *American Mineralogist*, *81*(9–10), 1297–1300.

Huppert, H. E., & Woods, A. W. (2002). The role of volatiles in magma chamber dynamics. *Nature*, *420*(6915), 493.

Hyman, D. M., Bursik, M., & Pitman, E. (2019). Pressure-driven gas flow in viscously deformable porous media: Application to lava domes. *Journal of Fluid Mechanics*, *869*, 85–109.

Jeffrey, D. J., & Acrivos, A. (1976). The rheological properties of suspensions of rigid particles. *AIChE Journal*, *22*(3), 417–432.

Jellinek, A. M., & Bercovici, D. (2011). Seismic tremors and magma wagging during explosive volcanism. *Nature*, *470*(7335), 522–525.

Johnson, J. B., Lyons, J. J., Andrews, B. J., & Lees, J. (2014). Explosive dome eruptions modulated by periodic gas-driven inflation. *Geophysical Research Letters*, *41*, 6689–6697. https://doi.org/10.1002/2014GL061310

Klug, C., & Cashman, K. V. (1996). Permeability development in vesiculating magmas: Implications for fragmentation. *Bulletin of Volcanology*, *58*(2–3), 87–100.

Kozono, T., & Koyaguchi, T. (2010). A simple formula for calculating porosity of magma in volcanic conduits during dome-forming eruptions. *Earth, Planets and Space*, *62*(5), 483–488.

Krieger, I. M., & Dougherty, T. J. (1959). A mechanism for non-Newtonian flow in suspensions of rigid spheres. *Transactions of the Society of Rheology*, *3*(1), 137–152.

LeVeque, R. J. (2002). *Finite volume methods for hyperbolic problems* (Vol. 31). Cambridge, UK: Cambridge University Press.
Lensky, N., Sparks, R., Navon, O., & Lyakhovsky, V. (2008). Cyclic activity at Soufrière Hills Volcano, Montserrat: Degassing-induced pressurization and stick-slip extrusion. *Geological Society, London, Special Publications*, *307*(1), 169–188.
Lyakhovsky, V., Hurwitz, S., & Navon, O. (1996). Bubble growth in rhyolitic melts: Experimental and numerical investigation. *Bulletin of Volcanology*, *58*(1), 19–32.
Manga, M. (1996). Waves of bubbles in basaltic magmas and lavas. *Journal of Geophysical Research*, *101*(B8), 17,457–17,465.
Mangan, M., & Sisson, T. (2000). Delayed, disequilibrium degassing in rhyolite magma: Decompression experiments and implications for explosive volcanism. *Earth and Planetary Science Letters*, *183*(3–4), 441–455.
Massol, H., & Jaupart, C. (1999). The generation of gas overpressure in volcanic eruptions. *Earth and Planetary Science Letters*, *166*(1–2), 57–70.
McKenzie, D. (1984). The generation and compaction of partially molten rock. *Journal of Petrology*, *25*(3), 713–765.
Melnik, O., & Sparks, R. (1999). Nonlinear dynamics of lava dome extrusion. *Nature*, *402*(6757), 37.
Michaut, C., Bercovici, D., & Sparks, R. S. J. (2009). Ascent and compaction of gas rich magma and the effects of hysteretic permeability. *Earth and Planetary Science Letters*, *282*(1–4), 258–267.
Michaut, C., Ricard, Y., Bercovici, D., & Sparks, R. S. J. (2013). Eruption cyclicity at silicic volcanoes potentially caused by magmatic gas waves. *Nature Geoscience*, *6*(10), 856–860.
Mori, J., White, R. A., Harlow, D. H., Okubo, P., Power, J. A., Hoblitt, R. P., et al. (1996). Volcanic earthquakes following the 1991 climactic eruption of Mount Pinatubo: Strong seismicity during a waning eruption. *Fire and Mud: Eruptions and Lahars of Mount Pinatubo, Philippines*, 339–350.
Murphy, M. D., Sparks, R. S. J., Barclay, J., Carroll, M. R., Lejeune, A.-M., Brewer, T. S., et al. (1998). The role of magma mixing in triggering the current eruption at the Soufriere Hills Volcano, Montserrat, West Indies. *Geophysical Research Letters*, *25*(18), 3433–3436.
Navon, O., Chekhmir, A., & Lyakhovsky, V. (1998). Bubble growth in highly viscous melts: Theory, experiments, and autoexplosivity of dome lavas. *Earth and Planetary Science Letters*, *160*(3–4), 763–776.
Owen, J., Tuffen, H., & McGarvie, D. W. (2013). Explosive subglacial rhyolitic eruptions in Iceland are fuelled by high magmatic H_2O and closed-system degassing. *Geology*, *41*(2), 251–254.
Parmigiani, A., Faroughi, S., Huber, C., Bachmann, O., & Su, Y. (2016). Bubble accumulation and its role in the evolution of magma reservoirs in the upper crust. *Nature*, *532*(7600), 492–495.
Pistone, M., Caricchi, L., Fife, J. L., Mader, K., & Ulmer, P. (2015). In situ X-ray tomographic microscopy observations of vesiculation of bubble-free and bubble-bearing magmas. *Bulletin of Volcanology*, *77*(12), 108.
Ribe, N. M. (1985). The deformation and compaction of partial molten zones. *Geophysical Journal International*, *83*(2), 487–501.
Ruprecht, P., & Bachmann, O. (2010). Pre-eruptive reheating during magma mixing at Quizapu Volcano and the implications for the explosiveness of silicic arc volcanoes. *Geology*, *38*(10), 919–922.
Rust, A., & Cashman, K. V. (2004). Permeability of vesicular silicic magma: Inertial and hysteresis effects. *Earth and Planetary Science Letters*, *228*(1–2), 93–107.
Rybczynski, W. (1911). Uber die fortschreitende bewegung einer flussigen kugel in einem zahen medium. *Bulletin International de l'Academie des Sciences de Cracovie A*, *1*, 40–46.
Saar, M. O., & Manga, M. (1999). Permeability-porosity relationship in vesicular basalts. *Geophysical Research Letters*, *26*(1), 111–114.
Sable, J., Houghton, B., Wilson, C., & Carey, R. (2006). Complex proximal sedimentation from Plinian plumes: The example of Tarawera 1886. *Bulletin of Volcanology*, *69*(1), 89–103.
Sahimi, M. (1994). *Applications of percolation theory*. London, UK: CRC Press.
Shaw, H. R. (1965). Comments on viscosity, crystal settling, and convection in granitic magmas. *American Journal of Science*, *263*(2), 120–152.
Šrámek, O., Ricard, Y., & Dubuffet, F. (2010). A multiphase model of core formation. *Geophysical Journal International*, *181*(1), 198–220.
Voight, B., Sparks, R., Miller, A., Stewart, R., Hoblitt, R., Clarke, A., et al. (1999). Magma flow instability and cyclic activity at Soufriere Hills volcano, Montserrat, British West Indies. *Science*, *283*(5405), 1138–1142.
Watamura, T., Iwatsubo, F., Sugiyama, K., Yamamoto, K., Yotsumoto, Y., & Shiono, T. (2019). Bubble cascade in Guinness beer is caused by gravity current instability. *Scientific Reports*, *9*(1), 5718.
Watson, I., Oppenheimer, C., Voight, B., Francis, P., Clarke, A., Stix, J., et al. (2000). The relationship between degassing and ground deformation at Soufriere Hills Volcano, Montserrat. *Journal of Volcanology and Geothermal Research*, *98*(1–4), 117–126.
Watts, R., Herd, R., Sparks, R., & Young, S. (2002). Growth patterns and emplacement of the andesitic lava dome at Soufriere Hills Volcano, Montserrat. *Geological Society, London, Memoirs*, *21*(1), 115–152.
Woods, A. W., & Koyaguchi, T. (1994). Transitions between explosive and effusive eruptions of silicic magmas. *Nature*, *370*(6491), 641–644.
Wylie, J. J., Voight, B., & Whitehead, J. (1999). Instability of magma flow from volatile-dependent viscosity. *Science*, *285*(5435), 1883–1885.
Yarushina, V. M., & Podladchikov, Y. Y. (2015). (De) compaction of porous viscoelastoplastic media: Model formulation. *Journal of Geophysical Research: Solid Earth*, *120*, 4146–4170. https://doi.org/10.1002/2014JB011258
Yokoo, A., Iguchi, M., Tameguri, T., & Yamamoto, K. (2013). Processes prior to outbursts of vulcanian eruption at Showa Crater of Sakurajima Volcano ([Special Section] Sakurajima Special Issue). *Bulletin of the Volcanological Society of Japan*, *58*(1), 163–181.
Zellmer, G., Sparks, R., Hawkesworth, C., & Wiedenbeck, M. (2003). Magma emplacement and remobilization timescales beneath montserrat: Insights from Sr and Ba zonation in plagioclase phenocrysts. *Journal of Petrology*, *44*(8), 1413–1431.